J. Fluid Mech. (1995), *vol.* 283, *pp.* 201–230

Surface-tension-driven Bénard convention at infinite Prandtl number

By A. THESS† AND S. A. ORSZAG
Program in Applied and Computational Mathematics, Princeton University, Princeton NJ, 08544, USA

(Received 6 December 1993 and in revised form 8 July 1994)

Surface-tension-driven convection in a planar fluid layer is studied by numerical simulation of the three-dimensional time-dependent governing equations in the limit of infinite Prandtl number. Emphasis is placed on the spatial scale of weakly supercritical flows and on the generation of small-scale structures in strongly supercritical flows. The decrease of the size of weakly supercritical hexagonal convection cells that we find is in agreement with experimental results. In the case of high Marangoni number, discontinuities of the temperature gradient are formed between convection cells, producing a universal spectrum $E \sim k^{-3}$ of the two-dimensional surface temperature field. The possibility of experimental verification is discussed on the basis of shadowgraph images calculated from the predicted hydrodynamic fields.

1. Introduction

This work is a numerical study of the simplest hydrodynamical model approximating the original experiments of Henri Bénard (1900*a*, *b*) on convection in fluid layers heated from below. More generally, the subject of this study is the convective flow in highly viscous fluids, like silicone oil, driven exclusively by thermocapillary forces. Although Bénard himself was aware of the important role of surface tension, it was not until the late 1950s that the dominance of surface forces in sufficiently shallow fluid layers was demonstrated both experimentally (Block 1956) and theoretically (Pearson 1958). In particular, Pearson has shown that the temperature dependence of the surface tension by itself is capable of producing an instability in a heated fluid layer that had hitherto been attributed to buoyancy forces only. Nevertheless, the overwhelming part of subsequent experimental and theoretical work has been focused on buoyancy-driven convection ('Rayleigh–Bénard convection') rather than on surface-tension-driven convection ('Bénard–Marangoni convection'). The former is observed either in deep layers or in fluid layers enclosed between two plates, where no free surface exists. For a comprehensive introduction to Bénard convection the reader is referred to the book of Koschmieder (1993) and to the review article of Normand, Pomeau & Velarde (1977).

The physical understanding of surface-tension-driven convection is far less advanced than of buoyancy-driven convection. In particular, numerical investigations of the strongly nonlinear Bénard–Marangoni problem have never been undertaken. Only one fully numerical study (Bestehorn 1993) exists for weakly nonlinear Bénard–Marangoni convection. Experimental studies in silicone oil under carefully controlled thermal and mechanical conditions have been carried out by Koschmieder (1967) and later by

† Permanent address and address for correspondence: Forschungszentrum Rossendorf, Postfach 510119, 01314 Dresden, Germany. Internet: thess@fz-rossendorf.de.

Koschmieder & Biggerstaff (1986), Koschmieder (1991) and Koschmieder & Switzer (1992) and provide an extensive background for numerical simulations. The main results of these experiments can be summarized as follows. In layers with thickness between 2 and 7 mm the critical temperature difference and the wavenumber of the instability agree with the linear theory of Nield (1964) which takes into account both surface tension and buoyancy forces. In a circular domain, the instability sets in as concentric rolls, which transform into a hexagonal convective structure after some transient time (Koschmieder 1967; Koschmieder & Biggerstaff 1986). If the thickness of the layer is less than 2 mm, convection appears for Marangoni numbers Ma far below the one predicted by Pearson (1958) and Nield (1964) with convective structures determined by the shape of the vessel. When the Marangoni number crosses the critical theoretical value, this subcritical pattern is replaced by hexagons (Koschmieder & Biggerstaff 1986). For slightly supercritical values of Ma, the cell size is a decreasing function of the temperature difference, in contrast to the increase of the cell size in Rayleigh–Bénard convection. The cell size in Bénard–Marangoni convection does not increase until Ma becomes higher than twice its critical value (Koschmieder 1991). The increase of the cell size in Bénard–Marangoni convection is attributed to the influence of gravity (Koschmieder & Switzer 1992). Several experimental investigations have been performed (Cerisier *et al.* 1987; Cerisier, Perez-Garcia & Occelli 1993, and references therein) in an attempt to understand the transition from a regular hexagonal pattern to increasingly disordered patterns, employing concepts from solid state physics, in particular ideas about order–disorder transition, melting, and defect dynamics. However, there is no control of the air above the fluid layer, which makes a fluid-dynamical interpretation of these results difficult. In order to completely eliminate the influence of gravity, two experiments were performed aboard Apollo 14 and Apollo 17 (Grodzka & Bannister 1972, 1975) where the gravity was less than $10^{-7}\,g$. The result was a demonstration of the generation of Bénard cells by surface tension alone, when gravity was virtually absent. However, the quantitative results derived from these experiments are open to serious doubt owing to severe drawbacks of the space experiment: The layer was not planar, and the heating was not stationary.

The results of the experiments raise a number of questions which cannot yet be answered by experiment alone: Do secondary effects like gravity, surface deformation and convection of air over the free surface have a significant influence on: (i) the selection of the hexagonal convective patterns, (ii) the decrease of the cell size for weakly supercritical flows, (iii) the existence of subcritical flow regimes? Furthermore, only a restricted range of Marangoni numbers was explored experimentally, leaving open the question about the existence of time-dependent or possibly turbulent surface-tension-driven flows for sufficiently high Marangoni numbers. Direct numerical simulation provides a convenient tool to answer the above questions by completely excluding the aforementioned secondary effects.

Theoretical studies of the thermocapillary Bénard problem have been focused on analytic and semi-analytic methods, i.e. linear stability analysis (Pearson 1958; Nield 1964; Scriven & Sternling 1964), energy stability theory (Davis 1969; Velarde & Castillo 1981) and bifurcation analysis (Scanlon & Segel 1967; Cloot & Lebon 1984; Bragard & Lebon 1993). Below $Ma = 56.77$ the system is unconditionally stable according to energy stability theory (Davis 1969). Above $Ma = 79.61$ the system becomes unstable with respect to infinitesimal perturbations with a wavenumber $k = 1.99$, as was demonstrated in the seminal paper of Pearson (1958) who assumed the free surface to be a non-deflecting boundary. Bifurcation theory, developed for the case of infinite Prandtl number by Scanlon & Segel (1967), predicts the selection of a

hexagonal convective pattern in favour of rolls slightly above the onset of instability. It also predicts that the hexagonal pattern remains stable for subcritical values of the Marangoni number as long as $(Ma-Ma_c)/Ma_c > -0.023$. The theory of Scanlon & Segel was generalized and partially corrected by Cloot & Lebon (1984) and by Bragard & Lebon (1993).

Although bifurcation theory has significantly improved our understanding of nonlinear Bénard–Marangoni convection, a mathematical inconsistency remains present in all bifurcation theories developed so far. On the one hand, the derivation of amplitude equations rests on the assumption that the amplitude of the bifurcated solution is $O(\epsilon^{1/2})$ where $\epsilon = (Ma-Ma_c)/Ma_c$. On the other hand, both quadratic and cubic nonlinearities are retained even though the coefficients of the quadratic terms are $O(1)$ which implies that the amplitude is $O(1)$, in contradiction to the foregoing assumption. Direct numerical simulation provides the opportunity to perform very precise computations of bifurcated finite-amplitude solutions. Cloot & Lebon (1984) were the first to address the question of wavenumber selection in nonlinear Bénard–Marangoni convection. They predicted that stable hexagonal convection patterns must have a higher wavenumber than the unstable mode, but they did not predict which wavenumber from the stable band will be selected. No investigation has been undertaken for Marangoni numbers far above the onset of instability. In a very recent paper Bestehorn (1993) has investigated the weakly nonlinear Bénard problem using amplitude equations and fully numerical simulation. The result of this work is a comprehensive understanding of amplitude and phase instabilities under the influence of both buoyancy and surface tension forces.

Considerable experimental and theoretical work has been devoted to thermocapillary phenomena in more complicated geometrics (spherical, cylindrical), to the influence of surface deformation, and to problems involving temperature gradients imposed along the free surface rather than perpendicular to it. The reader is referred to the excellent review article of Davis (1987) and to recent conference proceedings (Rath 1992; Velarde 1988) for more detailed information.

The aim of the present paper is to develop direct numerical simulations of the thermocapillary Bénard problem. The chief advantage of such an approach is the possibility to explore flows at zero gravity and high Marangoni number – conditions which are difficult to realize in laboratory experiments either on Earth or in Space. Owing to the simple geometry of the problem, straightforward application of spectral methods is possible which allows simulations with high precision. In the present paper we shall restrict our attention to the case of high Prandtl number fluids, which covers the vast majority of experiments on surface-tension-driven Bénard convection. The further restriction to the mathematical limit of infinite Prandtl number fluids leads to a conceptually simple model which allows a particularly efficient numerical implementation and, for certain values of the parameters, results in the numerical simulations proceeding faster than in real-life laboratory experiments.

Convection at infinite Prandtl number is of interest for the study of Earth-mantle convection, a slow motion on the timescale of millions of years. Numerical models of different levels of complexity have been employed for the study of this phenomenon (Schubert 1992), the simplest ones being very similar to the model to be used in our work (Vincent & Yuen 1988; Travis, Olson & Shubert 1990).

In the following section we summarize the physical assumptions of our theoretical model and derive the governing equations. In §3 we explain the numerical method. Sections 4 and 5 contain the results of our numerical simulations for weakly and strongly supercritical regimes, respectively. In §6 we demonstrate how numerical

simulations can be used to bridge the gap between theory and experiment by computing shadowgraph images from our numerically obtained temperature fields. Section 7 is devoted to a discussion of secondary effects and of further questions that would be useful to investigate. A preliminary account of the present work was published in Thess & Orszag (1994).

2. Governing equations

Consider a planar layer of fluid characterized by its thickness d, kinematic viscosity ν, thermal diffusivity κ, density ρ and surface tension σ. The layer is heated from below by a solid plate and has a free upper surface. The dynamics of the fluid is governed by the Navier–Stokes equation

$$\partial_t \boldsymbol{v} + (\boldsymbol{v}\cdot\boldsymbol{\nabla})\boldsymbol{v} = -\frac{\boldsymbol{\nabla} p}{\rho_0} + \nu\nabla^2\boldsymbol{v} + \frac{\boldsymbol{f}}{\rho_0}, \quad \boldsymbol{\nabla}\cdot\boldsymbol{v} = 0, \tag{1}$$

with force density $\boldsymbol{f}$, and by the heat conduction equation

$$\partial_t T + (\boldsymbol{v}\cdot\boldsymbol{\nabla})\, T = \kappa\nabla^2 T, \tag{2}$$

supplemented with appropriate initial and boundary conditions. There are two mechanisms which can bring the fluid into motion if the temperature field $T(x, y, z)$ differs from some constant value T_0. On the one hand, the *buoyancy force* $\boldsymbol{f} = \rho(x, y, z)\,\boldsymbol{g}$ is created due to the temperature dependence of the density which, in the framework of the Boussinesq approximation, can be written as

$$\rho = \rho_0 - \rho_0\,\alpha(T - T_0). \tag{3}$$

On the other hand, surface forces, called *thermocapillary forces*, are generated due to the temperature dependence of the surface tension which, again in the linear approximation, can be expressed as

$$\sigma = \sigma_0 - \gamma(T - T_0). \tag{4}$$

The thermal coefficient γ of the surface tension, usually positive, plays a central role in thermocapillary convection. The continuity of the tangential stresses across the free surface requires any temperature variation at the surface to be compensated by viscous stresses, and thereby by fluid motion. We are interested in a physical situation where thermocapillary forces dominate, and where the fluids have a high viscosity. In this case, the equations of motion can be greatly simplified. The following derivation is based on the consideration of the relevant timescales rather than on straightforward non-dimensionalization, since this approach provides a better physical insight into the problem.

The physical system is characterized by four different timescales. Whereas the viscous diffusion time

$$\tau_{visc} = d^2/\nu \tag{5}$$

and the thermal diffusion time

$$\tau_{th} = d^2/\kappa \tag{6}$$

are related to the molecular transport properties of the fluid, the buoyant timescale

$$\tau_b = (d/\alpha\Delta T g)^{1/2} \tag{7}$$

and the thermocapillary timescale

$$\tau_{tc} = (\rho_0\, d^3/\gamma\Delta T)^{1/2} \tag{8}$$

characterize the two driving forces. The buoyant timescale can be considered as the time which a hot blob of inviscid fluid, differing from its environment by a density defect $\delta\rho = \rho_0 \alpha \Delta T$, takes to travel across the layer. Indeed, the Lagrangian equation of motion $\rho_0 \ddot{x} = g\delta\rho$ for a small volume element directly yields the estimate (7). The thermocapillary timescale can be interpreted as the time needed to set into motion a hot spot of inviscid fluid with mass $m \sim \rho_0 d^3$ by an inhomogeneity $\delta\sigma = \gamma \Delta T$ of the surface tension. The estimate (8) is readily derived from the equation of motion $\rho_0 d^3 \ddot{x} = \delta\sigma d$. The timescales are usually combined to give the three dimensionless parameters

$$\text{Prandtl number} \qquad Pr = \frac{\tau_{th}}{\tau_{visc}} = \frac{\nu}{\kappa}, \tag{9}$$

$$\text{Rayleigh number} \qquad Ra = \frac{\tau_{visc}\tau_{th}}{\tau_b^2} = \frac{\alpha g d^3 \Delta T}{\nu\kappa}, \tag{10}$$

$$\text{Marangoni number} \qquad Ma = \frac{\tau_{visc}\tau_{th}}{\tau_{tc}^2} = \frac{\gamma d \Delta T}{\rho_0 \nu\kappa}. \tag{11}$$

Let us estimate the order of magnitude of these timescales for typical experimental conditions in shallow fluid layers such as encountered in the experiments of Bénard and his successors. When $d \sim 10^{-3}$ m, $\nu \sim 10^{-4}$ m^2 s^{-1} and $\kappa \sim 10^{-7}$ m^2 s^{-1}, then the viscous timescale is of the order of 0.1 s, whereas the thermal timescale is of the order of 10 s. Therefore we can assume

$$\tau_{visc}/\tau_{th} \to 0 \tag{12}$$

or, in other words, $Pr \to \infty$. This assumption is a good approximation for silicone oils in which $Pr = 100$–1000. It implies that the dynamics of the velocity field adjusts adiabatically to the time dependence of the temperature field, and that the time derivative in the Navier–Stokes equations can be neglected. Our second assumption,

$$\frac{\tau_{tc}}{\tau_b} = d\left(\frac{\rho_0 \alpha g}{\gamma}\right)^{1/2} \to 0, \tag{13}$$

or $Ra/Ma \to 0$ implies that surface forces dominate the dynamics of the fluid, and that gravity forces can be neglected. Under terrestrial conditions, the ratio Ra/Ma is roughly 0.25 for a layer of 1 mm thickness (and 2500 for a layer with $d = 10$ cm). Under microgravity conditions this ratio is of the order 10^{-8} for $d = 1$ mm. Note that dominance of thermocapillary forces can always be achieved in sufficiently shallow layers. The second assumption permits us to neglect the buoyancy term in the Navier–Stokes equation. An estimation of the Reynolds number of the flows in the experimental conditions on the basis of the observed typical velocities of $v < 10$ mm s^{-1} leads to the result that $Re = 10^{-1}$–10^{-3}. Therefore we can neglect the nonlinear term in the Navier–Stokes equation. It should be noted that the assumption of high Prandtl number does not automatically justify the omission of these terms, which may become important even if the dynamics of the fluid is slow or stationary. Finally, we assume an undeformed surface, which corresponds to the limit of strong surface tension. The validity of this assumption is a subtle question, discussed in depth by Scriven & Sternling (1964) and by Davis (1987). In the absence of gravity, the influence of surface deflection is characterized by the capillary number $C = \rho_0 \kappa\nu/\sigma_0 d$. The non-deflecting surface corresponds to the limit $C \to 0$. It was shown by Scriven & Sternling (1964) that weak surface deflection ($C \ll 1$) does not affect the critical Marangoni number except in the long-wave limit $k \to 0$. For weakly nonlinear convection the non-dimensional

d(mm)	Ma	C	Pr
1	51	5.1×10^{-3}	1000
2	102	2.6×10^{-3}	1000
3	153	1.7×10^{-3}	1000

TABLE 1. Marangoni number, capillary number and Prandtl number for a layer of silicone oil with depth d and $\Delta T = 10$ K, $\rho_0 = 968$ kg m^{-3}, $\sigma_0 = 1.9\times10^{-2}$ kg s^{-2}, $\gamma \simeq 5\times10^{-5}$ kg K^{-1} s^{-2}, $\nu = 10^{-4}$ m^2 s^{-1} $\kappa = 10^{-7}$ m^2 s^{-1}

surface deflection $h(x,y)/d$ is of the order $MaC = \gamma\Delta T/\sigma_0$. The values of the Marangoni number and of the capillary number for a layer of silicone oil at $\Delta T = 10$ K are listed in table 1. The value of $MaC = 2.6\times10^{-2}$ is very small in this case, which demonstrates that it is consistent to assume very small capillary number, large Prandtl number and Marangoni number of order unity.

As a result, we arrive at the following set of equations approximating the dynamics of an infinite Prandtl number fluid without gravity:

$$0 = -\nabla p + \nu\nabla^2 \boldsymbol{v}, \tag{14}$$

$$\nabla\cdot\boldsymbol{v} = 0, \tag{15}$$

$$\partial_t T + (\boldsymbol{v}\cdot\nabla)\,T = \kappa\nabla^2 T. \tag{16}$$

The boundary conditions for the flow field are the no-slip condition

$$v_x = v_y = v_z = 0 \quad \text{at} \quad z = 0, \tag{17}$$

and the so-called Marangoni boundary condition

$$\rho\nu\,\partial_z v_x = -\gamma\,\partial_x T, \tag{18}$$

$$\rho\nu\,\partial_z v_y = -\gamma\,\partial_y T, \tag{19}$$

$$v_z = 0 \tag{20}$$

at the free upper surface $z = d$. The conditions (18) and (19), expressing the continuity of the tangential stress across the free surface (Landau & Lifshitz 1987), are the decisive ingredient for surface-tension-driven convection. Indeed, they imply that any inhomogeneity of the surface tension due to variations of the surface temperature creates a shear at the free fluid surface. These conditions provide the link between the temperature field and the flow field. We shall assume that the bottom of the system is held at a constant temperature T_1, higher than the surface temperature $T_0 = T_1 - \Delta T$. For further convenience we introduce the temperature perturbation θ via

$$T = T_1 - (\Delta T/d)\,z + \theta. \tag{21}$$

The boundary condition at the bottom reduces then to $\theta = 0$. At the free surface we apply the boundary condition

$$\lambda_{th}\,\partial_z\theta = -\alpha_{th}\,\theta \tag{22}$$

with a heat transfer coefficient α_{th}. A comment is in order concerning this boundary condition. Strictly speaking, (22) is the definition of the phenomenological parameter α_{th} (see e.g. Landau & Lifshitz 1987) rather than a boundary condition. A derivation of (22) from first principles is only possible under the assumption that the heat loss is purely radiative, i.e. governed by the Stefan–Boltzmann law $\lambda_{th}\,\partial_z T = -ST^4$ ($S = 5.67\times10^{-8}$ W m^{-2} K^{-4}), and that θ is small, in which case $\alpha_{th} = 4ST_0^3$. Although

this 'vacuum assumption' is the only one leading to a well-defined constant heat transfer coefficient, phenomenological values of α_{th} can be used for experimental situations involving an air layer over the fluid surface in order to get order-of-magnitude estimates.

Introducing dimensionless variables of space, time, velocity and temperature obtained by dividing the physical variables by d, d^2/κ, κ/d, and ΔT, we obtain the following set of governing equations:

$$0 = -\nabla p + \nabla^2 \boldsymbol{v}, \tag{23}$$

$$\nabla \cdot \boldsymbol{v} = 0, \tag{24}$$

$$\partial_t \theta + (\boldsymbol{v} \cdot \nabla)\theta = v_z + \nabla^2 \theta, \tag{25}$$

$$T = -z + \theta, \tag{26}$$

with the boundary conditions

$$v_x = v_y = v_z = \theta = 0 \quad \text{at} \quad z = 0 \tag{27}$$

and

$$\partial_z v_x = -Ma\,\partial_x \theta, \tag{28}$$

$$\partial_z v_y = -Ma\,\partial_y \theta, \tag{29}$$

$$v_z = 0, \tag{30}$$

$$\partial_z \theta + Bi\,\theta = 0 \tag{31}$$

at $z = 1$, where the Biot number

$$Bi = \alpha_{th}\, d/\lambda_{th} \tag{32}$$

is a dimensionless measure of the heat loss. The boundary condition (31) permits us to express the Nusselt number as an integral over the surface temperature

$$Nu = 1 + \frac{Bi}{l_x l_y} \int \theta(x, y, 1)\, \mathrm{d}x\, \mathrm{d}y. \tag{33a}$$

For later convenience we shall use the scaled Nusselt number

$$\mathcal{N}u = (Nu - 1)/Bi \tag{33b}$$

which is a function of the surface temperature only and does not contain the Biot number. Finally, we assume periodic boundary conditions in the horizontal direction with arbitrary periodicity lengths l_x and l_y. For prescribed values of the parameters Ma, Bi, and the aspect ratios l_x and l_y, equations (23)–(26) and the boundary conditions (27)–(31) determine completely the velocity $\boldsymbol{v}(x, y, z, t)$ and the temperature perturbation $\theta(x, y, z, t)$. The rest of this paper is devoted to the numerical treatment of this system.

It is important to appreciate at the outset the central role of the temperature field $\theta_s(x, y)$ at the free surface. This field entirely determines the velocity field as can be verified by inspection of (23) and (24) and the boundary conditions (28)–(30). In infinite Prandtl number convection the velocity field does not have its own dynamics in the sense that it adjusts adiabatically to whatever input is provided by the surface temperature. The only nonlinear term in our equations is the convective term in the heat equation. A second remark is in order about the vertical vorticity $\omega = \partial_x v_y - \partial_y v_x$. This quantity is zero in the infinite Prandtl number limit, as can be readily verified by taking the curl of (23) and deriving the boundary conditions $\omega(0) = \partial_z \omega(1) = 0$ from (27)–(30). The only solution of the equation $\nabla^2 \omega = 0$ for the vertical vorticity is then the trivial one $\omega = 0$.

Let us briefly recall the physical mechanism of thermocapillary instability. Consider a local hot spot that has arisen at the surface due to a small deviation of the temperature from the basic state $\theta = 0$. Heat conduction tends to smooth out the spot, whereas thermocapillarity (cf. (28)) produces a radially outward flow above the spot which, by continuity, causes a vertical upflow to transport new hot fluid to the surface. These mechanisms counteract each other, and for sufficiently large temperature gradients, more precisely for $Ma > 79.6$ (for $Bi = 0$, $k = 1.99$), thermocapillary shear production ultimately dominates thermal diffusion and viscous dissipation, and thermocapillary convection ensues (Pearson 1958).

3. Numerical method

The system (23)–(31) is solved using a pseudospectral method (Canuto, Hussaini & Quarteroni 1987; Gottlieb & Orszag 1978) based on Fourier series in the horizontal directions and Chebyshev polynomial series in the vertical direction. The fact that the surface temperature determines the velocity field allows a very efficient solution of the Stokes problem (23) and (24) with the boundary conditions (27) and (28)–(30). If we denote the two-dimensional Fourier transform of the velocity and of the temperature by $\hat{v}_x(z)$, $\hat{v}_y(z)$, $\hat{v}_z(z)$ and $\hat{\theta}(z)$, and the horizontal wavenumber by $k^2 = k_x^2 + k_y^2$, the Stokes problem reduces to the equation

$$(\partial_z^2 - k^2)^2 \hat{v}_z = 0 \tag{34}$$

with the boundary conditions

$$\hat{v}_z(0) = \partial_z \hat{v}_z(0) = \hat{v}_z(1) = \partial_z^2 \hat{v}_z(1) + Mak^2\hat{\theta}(1) = 0 \tag{35a–d}$$

from which the horizontal velocity follows as

$$\hat{v}_x = \mathrm{i}\frac{k_x}{k^2}\partial_z \hat{v}_z, \quad \hat{v}_y = \mathrm{i}\frac{k_y}{k^2}\partial_z \hat{v}_z. \tag{36a, b}$$

Note that $\hat{v}_x$ and $\hat{v}_y$ automatically satisfy the boundary conditions (27)–(29), that the vertical vorticity is zero, and that the (time dependent) temperature enters the Stokes problem only through the Fourier amplitudes of the surface temperature in boundary condition (35d). Therefore we introduce velocity structure functions $\hat{v}_x^{(0)}$, $\hat{v}_y^{(0)}$ and $\hat{v}_z^{(0)}$ defined as solutions to the Stokes problem (34)–(36) with the boundary condition (35d) replaced by $\partial_z^2 \hat{v}_z^{(0)}(1) = -1$. These functions are precalculated at the beginning of each simulation using the Chebyshev-tau method and need only be multiplied with $Mak^2\hat{\theta}(1)$ to obtain the desired velocity field. Thus, the calculation of the velocity field requires $3N$ multiplications where N is the total number of collocation points. This figure should be compared with $38N$ multiplications necessary to solve the same problem including buoyancy force. In this case, the temperature field in the volume appears as an inhomogeneity in equation (34) which has then to be solved for each time step.

The application of the pseudospectral method to (25) is straightforward. The linear temperature terms are treated implicitly by the Crank–Nicolson time-differencing scheme, whereas the nonlinear term and the vertical velocity term are computed by the second-order Adams–Bashforth method.

The computations were performed on a parallel 32-processor IBM PVS 7245 computer. Our numerical method allows an efficient parallelization since the fast Fourier transform, necessary to compute the nonlinear term, is the only operation that requires communication between processors. At a resolution of $128^2 \times 32$ collocation

points, one time step requires only about 0.75 s of CPU time. Recall that the relevant thermal diffusion timescale in the experiments is of the order of minutes. For weakly supercritical conditions, more precisely for $Ma < 100$, our numerical code proceeds faster than a laboratory experiment and allows real-time simulations of pattern formation for aspect ratios as large as $l_x = l_y = 20$. For $Ma > 100$ smaller time steps must be taken, and the experiment becomes faster than the numerical simulation. For the highest value achieved here, $Ma = 2000$, 20 CPU hours are necessary to simulate one minute of the laboratory experiment.

The code has been tested in two different ways. First, we have tested whether the code reproduces correctly the primary instability described in Pearson's (1958) classical work. To this end, we have removed the nonlinear term, measured the growth rate of the primary Bénard–Marangoni instability of a roll with wavenumber $k = 2$ and compared it to the exact results derived in the Appendix. For $Ma = 80$, $Bi = 0$, a vertical resolution of 64 collocation points and time step $\mathrm{d}t = 10^{-3}$, we measure a growth rate of $\lambda = +0.029661914$ which differs from the exact value $\lambda = +0.029661942$ by a relative error of only 9.4×10^{-7}. For $Ma = 80$ and $Bi = 1$, we get the numerical value $\lambda = -2.495780$ to be compared with the theoretical growth rate $\lambda = -2.495744$. This test shows that all linear terms are accurately reproduced by our numerical scheme. In order to test the nonlinear term we have replaced the thermal boundary conditions by the zero-flux conditions $\partial_z \hat{\theta}(0) = \partial_z \hat{\theta}(1) = 0$. In this case, the integral over the temperature is a conserved quantity. Using

$$\theta = \theta_0 + \cos(2\pi x/l_x)\cos(2\pi z)$$

as an initial condition with the mean temperature θ_0 we find that this quantity is conserved with a precision of 10^{-6} in the course of temporal evolution.

The spatial resolution requirements are more severe in Bénard–Marangoni convection than in Rayleigh–Bénard convection because $v \sim \theta$ (cf. (35d)) while $v \sim \theta/k^2$ in Rayleigh–Bénard convection at infinite Prandtl number. Therefore, the Fourier amplitudes of the velocity are generally a factor k^2 larger in Bénard–Marangoni convection, and the nonlinear term involves high-wavenumber excitations. Therefore, with our presently available resolution, we are limited to the range $0 < Ma < 2500$ of Marangoni numbers.

4. The weakly nonlinear regime

4.1. *Pattern selection*

We shall first direct our attention to the case when the Marangoni number only slightly exceeds its critical value $Ma_c = 79.6$. Linear theory predicts an instability with respect to rolls with wavenumber $k_c = 1.99$, arbitrary horizontal direction and, of course, any superposition of such rolls. In order to predict the selected pattern, the nonlinear term must be taken into account which can be accomplished using either bifurcation theory (Scanlon & Segel 1967; Cloot & Lebon 1984) or direct numerical simulation. Our direct simulation approach offers the advantage that a much broader range of scales can be excited in the initial conditions thereby introducing virtually no *a priori* restrictions on the pattern, apart from the finite aspect ratio. We initialize the temperature field with an initial condition of the form.

$$\theta(x, y, z, 0) = \epsilon(x, y) z(2-z) \mathrm{e}^{-Biz}. \tag{37}$$

The field $\epsilon(x, y)$ with maximum and minimum values $\pm\epsilon$ is a random superposition of Fourier modes for all wavenumbers $k < \frac{1}{3}k_{max}$, where $k_{max} = \pi n_x/l_x = \pi n_y/l_y$ is the

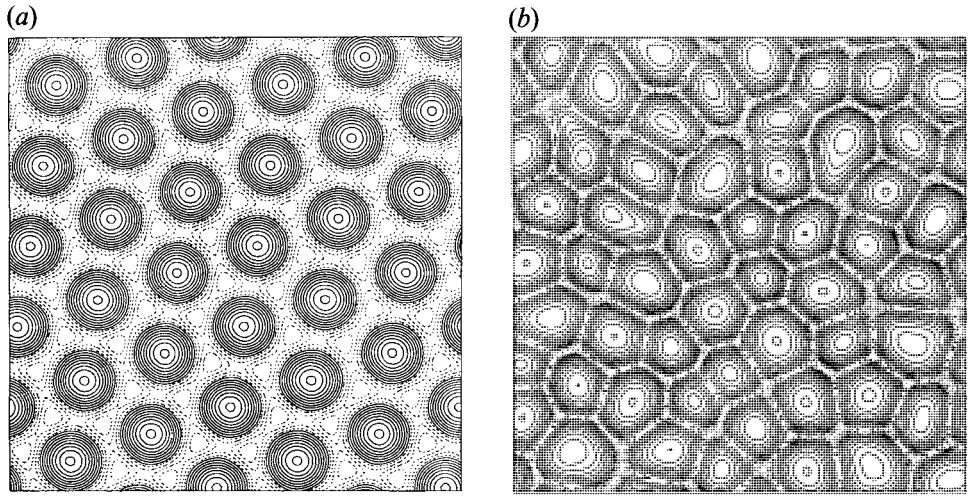

FIGURE 1. Surface temperature fields for weakly nonlinear Bénard convection: (*a*) for $Ma = 80$, $t = 1400$; (*b*) for $Ma = 150$, $t = 20$. The aspect ratio is 20 ($l_x = l_y = 20$), spatial resolution is $128^2 \times 32$, $\epsilon = 4 \times 10^{-3}$.

maximum horizontal wavenumber of the collocation method, and n is the number of collocation points in each horizontal direction. Most of the calculations have been done with $Bi = 0$ and aspect ratio $l_x = l_y = 20$.

The evolution of the system is characterized by three phases. In an initial phase, the unstable Fourier components grow on the timescale $\tau_{inst} = 1/\lambda$ given by the linear stability theory. This phase is followed by a nonlinear saturation of the instability after which a more or less regular pattern is formed, and the total kinetic energy of the flow reaches a stationary value. The relevant timescale for the second phase is again τ_{inst}. The third phase, taking place on the horizontal thermal diffusion timescale, is characterized by slow defect dynamics and wavenumber adjustment. We did not systematically analyse the long-lasting third phase of evolution, which can be more conveniently performed in the framework of amplitude equations. The reader is referred to Newell, Passot & Lega (1993) for a review of mathematical models of pattern formation and to the recent paper of Bestehorn (1993) for a detailed discussion of amplitude and phase instabilities in Bénard–Marangoni convection. We focus our attention here onto the end of the second phase, after which the nonlinear equilibration has taken place. In figure 1 we plot the surface temperature field for two different values of the Marangoni numbers after $t \approx 40\tau_{inst}$, when the kinetic energy has reached a stationary value. We have observed that the resulting pattern is perfectly regular as long as $Ma < 100$, while the disorder of the pattern increases rapidly if Ma becomes higher than 100. This is the first numerical simulation demonstrating the spontaneous formation of perfectly regular Bénard cells driven exclusively by thermocapillary forces. It is likely that the slightly disordered lattice obtained in the work of Bestehorn (1993) would have evolved to a perfectly ordered state if the simulations were continued for sufficiently long time.

The problem of planform selection in Bénard convection has long been a theoretical puzzle. A complete solution of this problem, at least for the weakly supercritical case, would require the demonstration that for arbitrary aspect ratio l_x and l_y, of the Biot number, and for all initial conditions the hexagonal planform is the stable attractor of the nonlinear governing equations. We have partially accomplished this task as

discussed next. In a series of numerical simulations for weakly supercritical conditions we have first checked that non-zero values of the Biot number ($Bi = 0.001$, 0.1, 1) do not affect the selection of the hexagonal planform. The only effect of the Biot number is to shift the critical Marangoni number and change growth rates of unstable modes as described in the Appendix. Secondly, we have examined the influence of the aspect ratios. Perfectly hexagonal patterns cannot fit into a rectangular domain unless the aspect ratios obey the relation $l_y/l_x = \sqrt{3}n/m$ or $l_x/l_y = \sqrt{3}n/m$ with integer n and m. Obviously, the square computational domain in figure 1 with $l_x = l_y = 20$ does not belong to this class. Nevertheless, the resulting pattern is almost indistinguishable from a perfectly hexagonal one. In order to understand the capability of the pattern to adapt to 'imperfect' aspect ratios, several computations were performed in a slightly distorted large-aspect-ratio domain with $l_x = 40 + \delta$ and $l_y = 40$. The simulations performed for $\delta = 0$, ± 0.1 and ± 0.5 show that the pattern retains its symmetry properties and adapts elastically to changes in the periodicity length. If one of the aspect ratios, say l_x, becomes very small, i.e. of the order of one, the hexagonal lattice is replaced by a row of rolls with axes parallel to the x-axis. This phenomenon, however, does not contradict the universality of the hexagonal pattern since it is due to the fact that the rolls compatible with the short periodicity length no longer belong to the linearly unstable band of wavenumbers. Finally, we have checked the sensitivity of the hexagonal lattice with respect to initial conditions. Replacing the random initial condition by a deterministic initial condition with square symmetry $\epsilon(x, y) \sim \sin(kx)\sin(ky)$ leads, after some transients, to a regular hexagonal pattern. Thus, our numerical results support the universality of the hexagonal planform in large-aspect-ratio Bénard–Marangoni convection.

Having characterized the ordered state, let us briefly discuss the degree of disorder in the patterns for increasing Marangoni number shortly after the end of the second phase of nonlinear equilibration. The degree of disorder in these 'intermediate' patterns, e.g. such as shown in figure 1(*b*), appears to be independent of the aspect ratios l_x and l_y, indicating that an explanation must be sought in terms of timescales characterizing a single convective cell. A possible explanation of this phenomenon may be given on the basis of the ratio between the instability timescale τ_{inst} and the vertical thermal diffusion time $\tau_{th} \sim 1$ if we assume that the nonlinear equilibration phase is characterized by local interactions between individual cells which occur within the vertical rather than the horizontal thermal diffusion timescale. In the case $Ma = 80$ (figure 1*a*) the instability timescale is about 30 times larger than the thermal timescale (see table 2 in the Appendix). Therefore, thermal diffusion has enough time to eliminate random fluctuations of the temperature, and a regular pattern is obtained as the final stationary state. For $Ma = 150$ (figure 1*b*), the instability timescale is approximately half the thermal diffusion time. In this case, the convective pattern is disordered in space. We conclude that the convective structure after nonlinear equilibration is hexagonal without any defects in the interval $79.6 < Ma < 100$, where $\tau_{inst} > \tau_{th}$, and defects are not present until $Ma > 100$. It should be emphasized that this is a fairly rough criterion for two reasons. On the one hand, the definition of the duration of the second evolution phase involves some ambiguity. On the other hand, a pattern which is disordered after nonlinear saturation does not necessarily remain disordered forever. A systematic investigation of the disorder in the third evolution phase would require very long simulations in large-aspect-ratio geometries with Marangoni numbers increased by small steps, which is unfortunately beyond our present numerical capabilities. The question whether the long-time evolution leads finally to a perfect hexagonal pattern was studied in the experimental work of Occelli, Guazzelli &

Pantaloni (1983). They found an increasing number n_d of defects for increasing Ma, approximately described by the 'Arrhenius law' $n_d \sim \exp(-A/\epsilon)$ with $\epsilon = (Ma - Ma_c)/Ma_c$. Therefore, a perfectly hexagonal pattern must be considered as a metastable state for $Ma > 100$, with the tendency to develop defects as a result of small perturbations. Observation of perfectly hexagonal patterns by Koschmieder & Switzer (1992) for Marangoni numbers of twice Ma_c does not contradict this statement, because great care was taken in these experiments to eliminate all kinds of thermal and mechanical perturbations.

4.2. *Properties of single hexagons and rolls*

Having identified hexagons as the dominating structures for weakly supercritical conditions, we turn to a more detailed characterization of a single hexagonal cell. In addition, we consider the properties of convection rolls for two reasons. On the one hand, quasi-one-dimensional convective patterns dominate in linear strips or in annuli when the transverse width $l_y \ll l_x$ and $l_y \sim 1$. In some respects, such a situation is similar to the conditions in the experiments of Bensimon (1988), although the appearance of a one-dimensional pattern in this case is likely to be a result of boundary conditions at lateral walls. On the other hand, the computation of the Nussel number allows us to compare the efficiency of heat transfer and to assess the role of the dimensionality of the flow. We numerically investigate single hexagons and rolls by a method similar to that used in experiments. Starting with an initial perturbation (37) with a deterministic function $\epsilon(x, y)$ with the symmetry of hexagons or rolls, we proceed with the calculation until a stationary flow is established. Then the Marangoni number is either decreased or increased by a small amount taking the last temperature field as the initial condition for the new simulation. Since we are not far away from the onset of instability, these measurements can be performed quickly, and we can even change parameters such as the periodicity length of the convective structures or the Biot number, which can be hardly achieved in an experiment.

For each stationary solution we determine the kinetic energy

$$E_v = \frac{1}{2l_x l_y} \int \boldsymbol{v}^2 \, \mathrm{d}^3 \boldsymbol{x}, \tag{38}$$

the 'thermal energy'

$$E_\theta = \frac{1}{2l_x l_y} \int \theta^2 \, \mathrm{d}^3 \boldsymbol{x} \tag{39}$$

and the scaled Nussel number

$$\mathcal{N}u = \frac{1}{l_x l_y} \int \theta_s \, \mathrm{d}^2 \boldsymbol{x} \tag{40}$$

where θ_s is the surface temperature. The results of the numerical experiments are summarized in figure 2, where we plot E_v, E_θ and $\mathcal{N}u$ for hexagons and rolls as a function of the Marangoni number. At $Ma = 79.6$ the hexagonal cell bifurcates subcritically from the purely conductive state. The subcritical regime extends down to $Ma_s = 79.0$. The extension of the subcritical range $(Ma_s - Ma_c)/Ma_c = -0.0075$ should be compared with the prediction $(Ma_s - Ma_c)/Ma_c = -0.023$ of Scanlon & Segel (1967), based on bifurcation theory for an infinite Prandtl number fluid with $d \to \infty$. Given the highly simplifying assumption of infinite layer thickness, the quality of the prediction of bifurcation theory is remarkably good. Although the results of the model cannot be directly compared to our numerical findings, the kinetic energy per unit area of the hexagonal pattern as predicted by bifurcation analysis is in qualitative

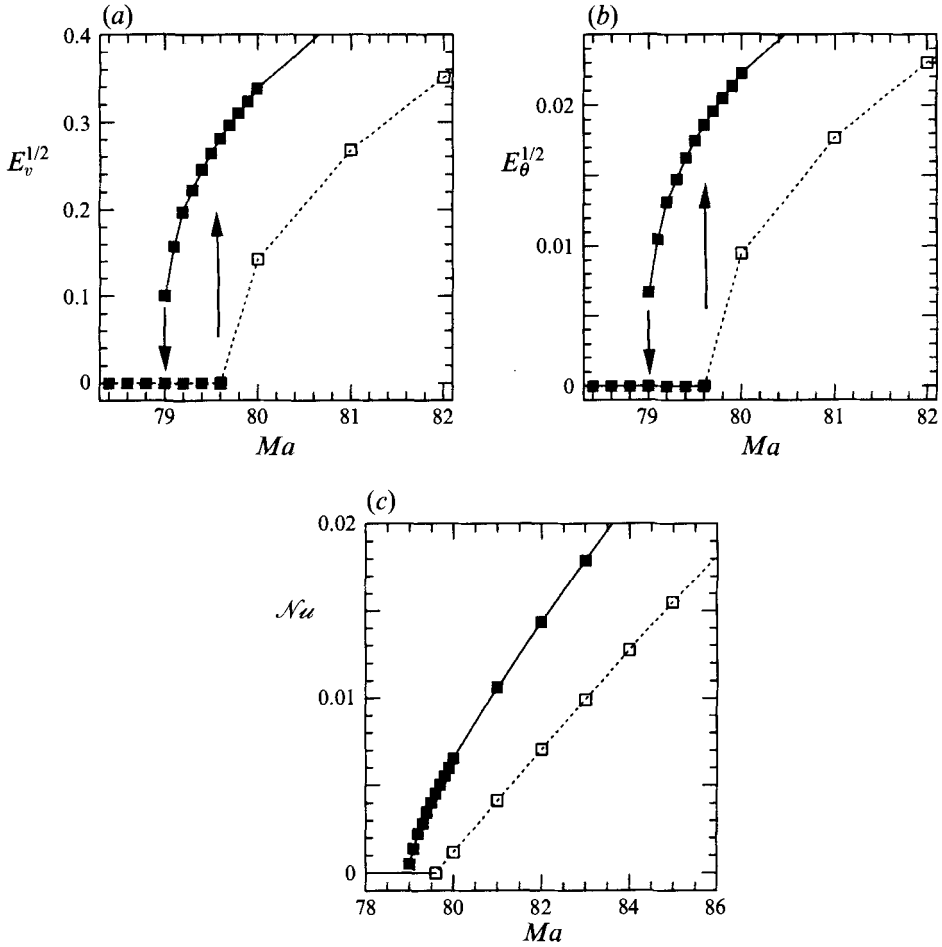

FIGURE 2. Stationary hexagons and rolls: (*a*) integral velocity $v = E_v^{1/2}$, (*b*) integral temperature perturbation $\theta = E_\theta^{1/2}$, (*c*) Nusselt number as a function of the Marangoni number. Spatial resolution is $32 \times 64 \times 32$ for hexagons and 32^3 for rolls. $l_x = l_y = 2\pi/k_c$ for rolls and $l_x = 4\pi/\sqrt{3}k_c$, $l_y = 4\pi/k_c$ for hexagons with $k_c = 1.9929$. Solid squares: hexagons, open squares: rolls.

agreement with our numerical values. The bifurcation approach was recently extended to finite layer thickness by Bragard & Lebon (1993). The calculated extension $(Ma_s - Ma_c)/Ma_c = -0.0056$ of the subcritical domain appears to be in good agreement with our numerical result.

The square roots of E_v and E_θ, plotted in figures 2(*a*) and 2(*b*), can be considered as 'integral velocity' and 'integral temperature' scales. Since the velocity and temperature peak at the free surface, the integral scales underestimate the maximum velocity and temperature perturbation by approximately one order of magnitude. Nevertheless, that permits us to estimate the Reynolds and Péclet numbers characterizing the importance of nonlinear terms in the Navier–Stokes equation and in the heat conduction equation. From the data of figure 2(*a*) the integral Reynolds number of the supercritical flow is evaluated as

$$Re \sim E_v^{1/2}/Pr, \tag{41}$$

yielding $Re \sim 6 \times 10^{-4}$ for $Ma = 80$ and $Pr = 1000$. Thus, the omission of the nonlinear

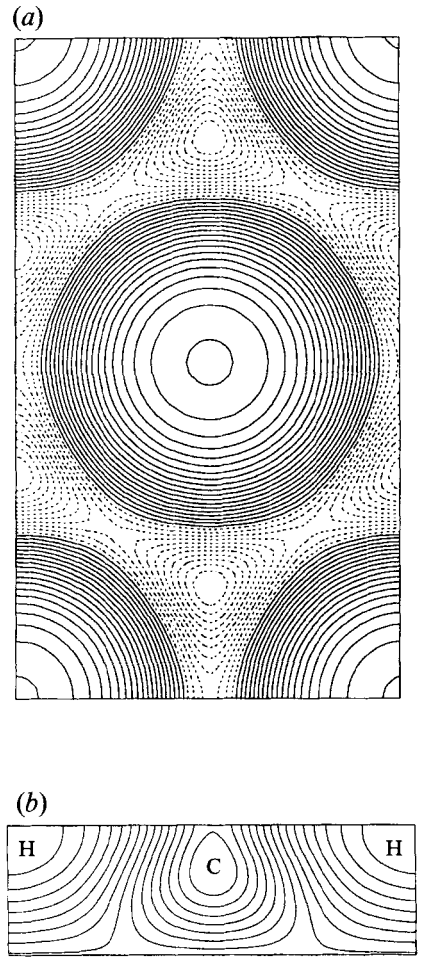

FIGURE 3. (*a*) Surface temperature field $\theta_s(x, y)$ of a stationary hexagon at $Ma = 100$, (*b*) temperature slice $\theta(x, z)$ of a roll at $Ma = 100$. Numerical parameters as in figure 2.

term from the Navier–Stokes equation is justified *a posteriori*. The integral Péclet number $Pe = vd/\kappa$, characterizing the deformation of the temperature isolines due to convective motion, is

$$Pe \sim E_v^{1/2} \tag{42}$$

with $Pe = 0.15$ for $Ma = 80$. The surface Péclet number evaluated with the maximum velocity at the free surface is thus already of the order of one for weakly supercritical flows. Note that the Marangoni number is a Péclet number based on the thermocapillary velocity scale $v = \gamma \Delta T/\rho\nu$. The plot of the Nusselt number in figure 2(*c*) shows that hexagons are more efficient in enhancing heat transfer than rolls. The deformation of the temperature isolines due to convective motion is highlighted in figure 3, where we plot the surface temperature of a hexagon together with a slice of the temperature field of a roll. Nonlinear effects lead to an expansion of the region of hot upwelling fluid at the expense of cold regions, as seen by comparison of the hexagon in figure 3(*a*) with the hexagonal lattice depicted in figure 1(*a*). Figure 3(*b*) shows that the isotherms become compressed in the cold region underneath the free surface.

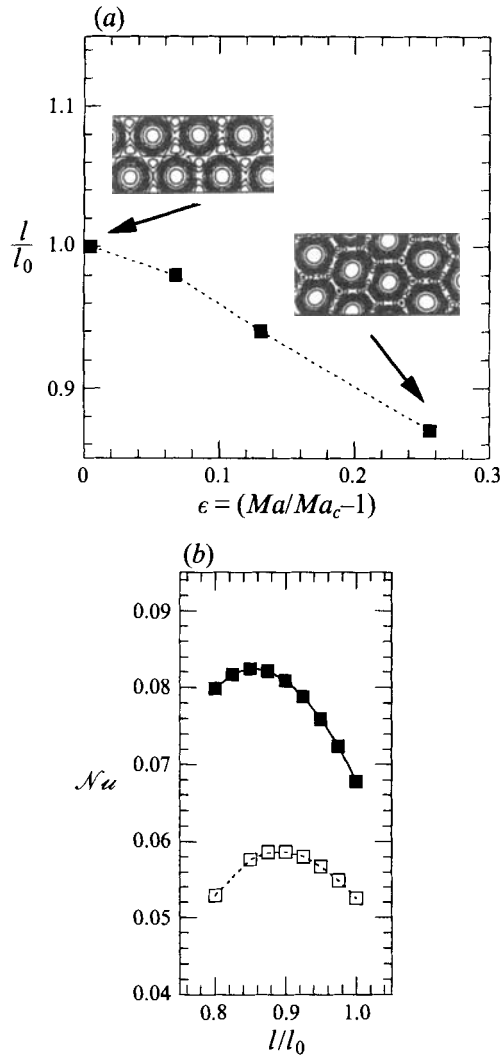

FIGURE 4. Decreasing cell size in Bénard–Marangoni convection. (*a*) Dimensionless lengthscale of hexagonal cells as a function of the Marangoni number. Spatial resolution is $512 \times 16 \times 16$ for $\epsilon < 0.2$ and $1024 \times 32 \times 16$ for $\epsilon > 0.2$, $l_x = 50 \times 4\pi/\sqrt{3}k_c$, $l_y = 4\pi/k_c$, $k_c = 1.9929$. (*b*) Nusselt number as a function of the periodicity length for hexagons (solid squares) and rolls (open squares) for $Ma = 100$. Spatial resolution and domain size as in figure 2.

4.3. *The wavelength of supercritical hexagonal cells*

The variation with Marangoni number Ma of the size of weakly supercritical hexagonal patterns, which is of fundamental fluid-dynamic interest, has conflicting experimental results. While Koschmieder & Switzer (1992) observe decreasing cell size, Cerisier *et al.* (1987) report a monotonic increase of the cell size as a function of Ma for larger values of Ma.

A straightforward way to numerically determine the wavenumber $k(Ma)$ of supercritical patterns would be to conduct simulations at large aspect ratio, and to measure the density of cells as a function of the Marangoni number. In order to obtain accurate numerical results, which are not contaminated by finite-size effects, computations with aspect ratio 100 and total integration time of the order of the lateral

thermal diffusion time (10^4 in units of d^2/κ) would be necessary. The large aspect ratio is necessary because the smallest change of lengthscale which can be detected is $\Delta l_0/l_0 \sim n^{-1}$ where n is the number of convective cells in each spatial direction. Thus, $n \sim 100$ is necessary to detect contractions or dilatations of the pattern with a precision of 1 %. This task is quite expensive computationally, although our numerical method is capable of handling aspect ratios as large as 40 (comprising about 200 convection cells) in the considered parameter region. There is, however, an efficient alternative providing an unambiguous answer as to whether supercritical hexagonal cells are expanding or shrinking with increasing temperature. The method consists in performing the simulation in a quasi-one-dimensional domain which is sufficiently long in the x-direction to accommodate a multitude of hexagons, and which is sufficiently short in the y-direction for thermal equilibrium to proceed within the transverse ($O(1)$) thermal diffusion timescale. We have chosen a strip with length $l_x = 182.02$ and $l_y = 6.305$ which comprises 50 elementary domains of the type depicted in figure 3(a). We initialize the temperature field with random initial conditions and count the number N of cells after the system has settled to an ordered state consisting of hexagonal cells. For $Ma = 80$ we obtain $N = 100$, corresponding exactly to the number of cells associated with the wavenumber $k_c = 1.99$ of the first unstable mode. These cells are arranged in two rows, a part of which is shown in the upper insert of figure 4(a). Repeating the computations with increasing Ma, we evaluate the dimensionless lengthscale $l/l_0 = N_0/N$, under the condition that the system consists of two rows of cells. The use of up to 1024 collocation points in the x-direction, corresponding to about 20 Fourier modes per convection cell, ensures high numerical precision (at the expense of long simulation time).

As the Marongoni number is increased, we observe a compression of the pattern in the x-direction which leads to a deformation of the equilateral triangles formed by the centres of the cells. As a result, the number of cells increases and their lengthscale decreases, as is seen in figure 4(a). Note that the system cannot continuously shrink in the transverse direction owing to the small transverse aspect ratio. The latter process proceeds discontinuously, as seen from the bend of the curve in figure 4(a). For $\epsilon > 0.1$ the cell size has sufficiently decreased for the cells to fit into the strip as an aligned arrangement, depicted in the lower insert of figure 4(a), rather than the staggered arrangement (upper insert in figure 4a). Then, the lengthscale decreases again continuously. The numerical results plotted in figure 4(a) demonstrate unambiguously that the cell size in weakly supercritical high Prandtl number surface-tension-driven convection is a monotonically decreasing function of the temperature. Therefore, our results support the experimental results of Koschmieder & Switzer (1992).

For Marangoni numbers higher than 100, corresponding to the highest ϵ in figure 4(a), defects survive even after long evolution time, and a precise determination of the cell size becomes impossible. For $Ma > 100$, we visually observe that the 'integral scale' of the convective structures continues to decrease until a saturation is reached when the cell size is of the order of the layer thickness.

From figure 4(a) we can derive the result that $\mathrm{d}(l/l_0)/\mathrm{d}\epsilon \approx -0.5$, which can be interpreted as a (negative) coefficient characterizing the variation of wavelength of hexagons. This value, however, cannot be directly compared to the experimental one $\mathrm{d}(l/l_0)/\mathrm{d}\epsilon = Ma_c\,\mathrm{d}(k_c/k)/\mathrm{d}Ma \approx = -0.14$ of Koschmieder & Switzer (1992) (at aspect ratio 55) since our coefficient describes the contraction of a transversely constrained system, whereas the experimental pattern is free in both directions. The situation is rather similar to the measurement of thermal expansion coefficients of liquids: the

radius of a spherical drop increases as $\mathrm{d}(R/R_0)/\mathrm{d}T = \frac{1}{3}\alpha$ whereas the length of a fluid column enclosed in a pipe increases three times faster, i.e. as $\mathrm{d}(L/L_0)/\mathrm{d}T = \alpha$, where α is the thermal expansion coefficient of the fluid. Therefore our coefficient should be divided by two in order to estimate the variation of wavelength of an unconstrained two-dimensional pattern as -0.25. The difference with the experimental result may be due to the influence of buoyancy force, present in the experiments, so that (as already noted by Koschmieder & Switzer) the wavenumber k is a function of both Ma and Ra and the measured value $\mathrm{d}k/\mathrm{d}Ma = \partial k/\partial Ma + (\mathrm{d}Ra/\mathrm{d}Ma)_{k=\mathrm{const}}\,\partial k/\partial Ra$ is a superposition of the pattern contraction due to thermocapillarity and the pattern expansion due to buoyancy. The influence of the buoyancy term is reinforced by the high value of $(\mathrm{d}Ra/\mathrm{d}Ma)_{k=\mathrm{const}}$ which is roughly proportional to the slope of the neutral stability curve $\mathrm{d}Ra/\mathrm{d}Ma \sim -10$ calculated by Nield (1964). Therefore even a weak influence of gravity can affect the wavenumber of Bénard–Marangoni convection.

The analogy between the contraction of the hexagonal pattern and the compressibility of fluids is not entirely fortuitous. We have observed that the longitudinal distance between the cells decreases [increases] when we increase [decrease] the transverse width by a factor of 1.02 [0.98], keeping the Marangoni number fixed. Thus, the convection pattern has the property of elasticity.

Finally we wish to make a remark about the validity of the 'maximum heat transfer' hypothesis in thermocapillary convection, which states that the selected wavenumber of supercritical flow is the one maximizing the Nusselt number at a given Ma. In figure 4(*b*) we plot the Nusselt number as a function of the size of a single hexagon and a single roll for $Ma = 100$. The figure clearly shows that in thermocapillary-driven convection smaller structures provide a more efficient heat transfer, although the location of the maximum of the Nusselt number does not coincide with the observed wavelength of the cells. The maximum heat transfer assumption does not hold in Rayleigh–Bénard convection, where the observed wavelengths are not the wavelengths which transfer the most heat.

5. The strongly nonlinear regime

5.1. *Phenomenology*

In isothermal fluids it has proven fruitful to consider the behaviour of fluids in the limit of infinite Reynolds number (or $\nu \to 0$) when molecular viscosity becomes irrelevant for the large-scale properties of the flow. In non-isothermal fluids there are two molecular transport coefficients, i.e. the viscosity and the thermal diffusivity, and the related dimensionless parameters $Re = ul/\nu$ and $Pe = ul/\kappa$. Different kinds of turbulent flows develop depending on which of these parameters tends to infinity. Here we are interested in the flow for high Marangoni numbers and infinite Prandtl number which corresponds to $Re \to 0$ and $Pe \to \infty$. This case strongly differs from the 'hard Rayleigh–Bénard turbulence' (Castaign *et al.* 1989) in which both $Re \to \infty$ and $Pe \to \infty$. In our case, the flow is still dominated by viscosity, while the temperature isolines get strongly deformed and the thermal diffusivity can be neglected except in thin thermal layers of thickness $\delta \sim 1/Pe$. It is known both from experiments (Whitehead & Parsons 1978) and from numerical simulations (Vincent & Yuen 1988; Travis *et al.* 1990) of Rayleigh–Bénard convection at infinite Prandtl number, that the velocity field and the temperature field exhibit non-trivial small-scale behaviour in the limit of high Rayleigh number (and thus $Pe \gg 1$). Here we shall consider the analogous question for thermocapillary-driven Bénard convection at high Marangoni number.

The plot given in figure 5 provides a first glimpse of the generation of small scales

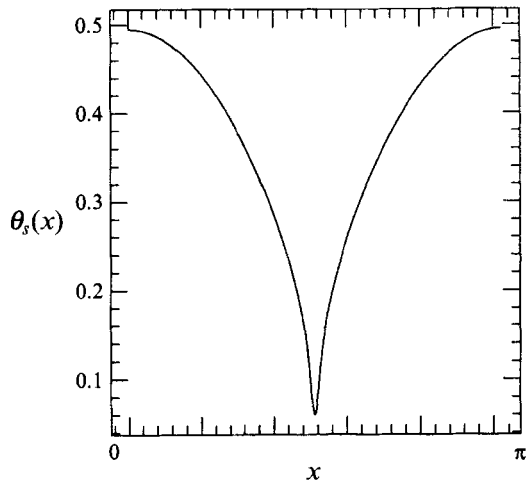

FIGURE 5. Strongly nonlinear Bénard–Marangoni convection: surface temperature field of a single roll. Spatial resolution is $512 \times 32 \times 128$, $l_x = \pi$, $l_y = 1$, $Ma = 2000$.

in Bénard–Marangoni convection, showing the surface temperature field of a single roll at $Ma = 2000$. The temperature field consists of parabolic regions separated by increasingly sharp transition layers at the cell boundary, where the temperature gradient experiences a discontinuity. The width of these layers is of the order of $\delta \sim 1/Pe$. The Péclet number, estimated on the basis of the maximum surface velocity difference, is of the order of 100 for the roll shown in figure 5. Note that the Reynolds number is still as small as 0.1 if the fluid has $Pr = 1000$. The first derivative of the surface temperature resembles the sawtooth structure of solutions to the Burgers equation $u_t + uu_x = \nu u_{xx}$ in the limit $\nu \to 0$. The second derivative of the surface temperature consists of a sharp spike, nearly a delta function, at the location of the transition layer embedded in a smooth background. Indeed, the two-dimensional Laplacian of the surface temperature $\Delta_2 \theta_s \equiv \partial_x^2 \theta_s + \partial_y^2 \theta_s$ is well suited to focus on the characterization of small-scale structures and shall be used in the following for visualization purposes. Moreover, this quantity is closely related to shadowgraph images as discussed in §6. We have noted in the preceding section that the Péclet number increases rapidly even for weakly supercritical values of Ma. Therefore, the generation of small scales can already be seen in convective flows at modest Marangoni number, such as $Ma = 150$. This is demonstrated in figure 6 (plate 1), where we plot the two-dimensional Laplacian of the surface temperature. Blue [red] regions of $\Delta_2 \theta_s$ correspond to negative [positive] curvature of the surface temperature field θ_s. For $Ma = 80$ (figure 6*a*) the field is essentially a superposition of three unstable modes of the linear theory. Indeed, the surface Péclet number in figure 6(*a*) is of the order of one, while it is 10 for $Ma = 150$. For $Ma = 150$, figure 6(*b*) shows that the higher velocity leads to a nonlinear redistribution of the temperature gradients. Narrow thermal boundary layers, characterized by strong positive curvature of the temperature field, are embedded in a smooth background. One important difference with one-dimensional rolls (figure 5) is the existence of points at which three thermal boundary layers coalesce and form strong local maxima of the curvature. In the vicinity of such a point the three-dimensional temperature field has the structure of a thermal plume, a localized object frequently encountered in thermal convection. The curvature maxima are seen as red spots in figure 6(*b*). They are the key features for understanding the spectrum of the surface temperature as will be shown in the next section.

Note that there is a resemblance between the nonlinear evolution of surface temperature and solutions to the two-dimensional modified Burgers equation

$$\partial_t \phi - (\nabla \phi)^2 = \nu \Delta_2 \phi \tag{43}$$

which can be understood by evaluating the heat conduction equation (25) at the free surface. With free surface quantities denoted by an index s, (25) gives

$$\partial_t \theta_s + (\boldsymbol{v}_s \cdot \nabla)\theta_s = \Delta_2 \theta_s + (\partial_z^2 \theta)_s. \tag{44}$$

Recall that $v_{zs} = 0$, and that $\boldsymbol{v}_s$ is parallel to the surface. Since the velocity is governed by a linear elliptic system of partial differential equations with $\boldsymbol{v} = 0$ at the bottom and an inhomogeneous boundary condition for $\boldsymbol{v}$ at $z = 1$, the horizontal velocity assumes its maximum at the free surface. Therefore, the vertical derivative $\partial_z \boldsymbol{v}_s$ is roughly proportional to $\boldsymbol{v}_s$, and the Marangoni boundary condition (28), (29) becomes

$$v_{xs} \sim -Ma\, \partial_x \theta_s, \tag{45}$$

$$v_{ys} \sim -Ma\, \partial_y \theta_s. \tag{46}$$

Thus, $\boldsymbol{v}_s \sim -Ma \nabla \theta_s$, from which derives the similarity to the nonlinear term of the Burgers equation.

5.2. *The spectrum of surface temperature*

In order to understand the partition of energy between the macroscale l (cell size) and the microscale δ (width of the thermal boundary layers) we consider the spectrum

$$E(k) = \sum_{k-\Delta k < |\boldsymbol{k}| < k+\Delta k} \langle \hat{\theta}_s(\boldsymbol{k})\, \hat{\theta}_s^*(\boldsymbol{k}) \rangle, \tag{47}$$

defined as an ensemble average of the complex Fourier amplitudes of the surface temperature. Here $\boldsymbol{k} = (k_x, k_y)$ is the two-dimensional vector of horizontal wavenumbers. Since the temperature field is virtually time-independent after the process of nonlinear equilibration, we perform several independent runs with different realizations of the random initial conditions. After a prescribed evolution time, the Fourier amplitudes are normalized and the average (47) is evaluated. In figure 7 we plot two different realizations of $\Delta_2 \theta_s$ for $Ma = 2000$. Figure 8 shows the spectrum $E(k)$ for one single surface field. In the 'inertial range' $1/l < k < 1/\delta$ this spectrum shows a power-law behaviour $E \sim k^{-\alpha}$ with an exponent close to 3. We have determined $\alpha = 3.1$ from a linear regression on $E(k)$ in the range $0.7 < \log(k) < 1.4$ obtained as the ensemble average over three runs. An explanation of this temperature spectrum, which we found to be insensitive to initial conditions, to the value of the Biot number as well as to the specific value of Ma, can be given employing ideas from ordinary fluid turbulence, specifically Saffman's theory of two-dimensional turbulence.

Saffman (1971) assumes discontinuities of the vorticity, a first velocity derivative, to be key features of two-dimensional turbulence. He conjectures the palinstrophy, a second velocity derivative, to be a random arrangement of one-dimensional delta functions. Such a function has a flat energy spectrum from which Saffman derives an $E \sim k^{-4}$ spectrum of kinetic energy. In the present case, discontinuities of the surface temperature gradient between contiguous cells are formed as a result of the high Péclet number. Thus, the second temperature derivative $\Delta_2 \theta_s$ is composed of *one-dimensional* delta-functions as highlighted in figure 7. At first glance, these features seem to suggest an $E \sim k^{-4}$ spectrum in analogy to the Saffman theory. The key to the understanding of the observed k^{-3} law, however, is the plumes at which three thermal boundary layers merge. At these points, $\Delta_2 \theta_s$ behaves like a *two-dimensional* delta-function in contrast to the isolated thermal layers, which requires a modification of Saffman's arguments. We can assume that the field $\Delta_2 \theta_s$ is dominated by an irregular distribution of delta-

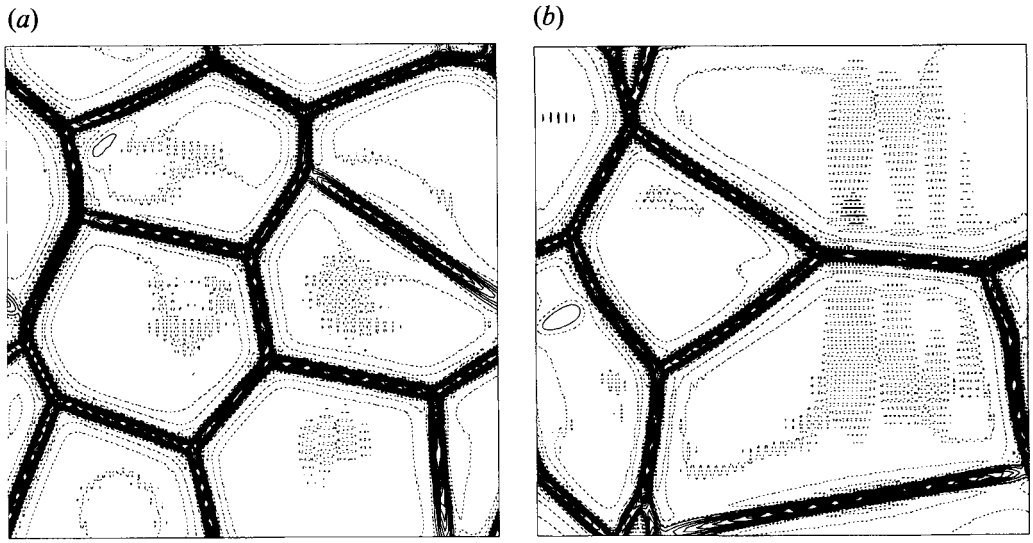

FIGURE 7. Two fields $\Delta_2\theta_s(x,y)$ evolving from different realizations of the random initial conditions for $Ma = 2000$ after $t = 0.07$. Aspect ratios is 3, spatial resolution $128^2 \times 64$.

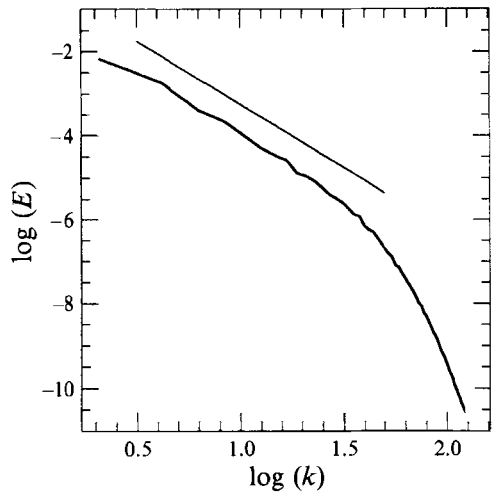

FIGURE 8. Spectrum of surface temperature for a single realization for $Ma = 2000$. The line $E \sim k^{-3}$ is drawn to guide the eye.

functions with the density N of the order of the basic wavenumber of the pattern and with intensities J_i over the plumes, i.e.

$$\Delta_2\theta_s = \sum_i J_i\,\delta(\boldsymbol{r}-\boldsymbol{r}_i)\,N\bar{J}. \tag{48}$$

The contribution from the one-dimensional thermal boundary layers leads to a steeper spectrum, so it can be neglected. In order to calculate the energy spectrum of θ_s we must consider the correlation function of $\Delta_2\theta_s$ which has the form

$$\langle\Delta_2\theta_s(\boldsymbol{r})\,\Delta_2'\theta_s(\boldsymbol{r}')\rangle = \frac{N\overline{J^2}}{4\pi^2}\int e^{i\boldsymbol{k}(\boldsymbol{r}-\boldsymbol{r}')}\,d^2k - \frac{(N\bar{J})^2}{2}\int\delta(\boldsymbol{k})\,e^{i\boldsymbol{k}(\boldsymbol{r}-\boldsymbol{r}')}\,d^2k. \tag{49}$$

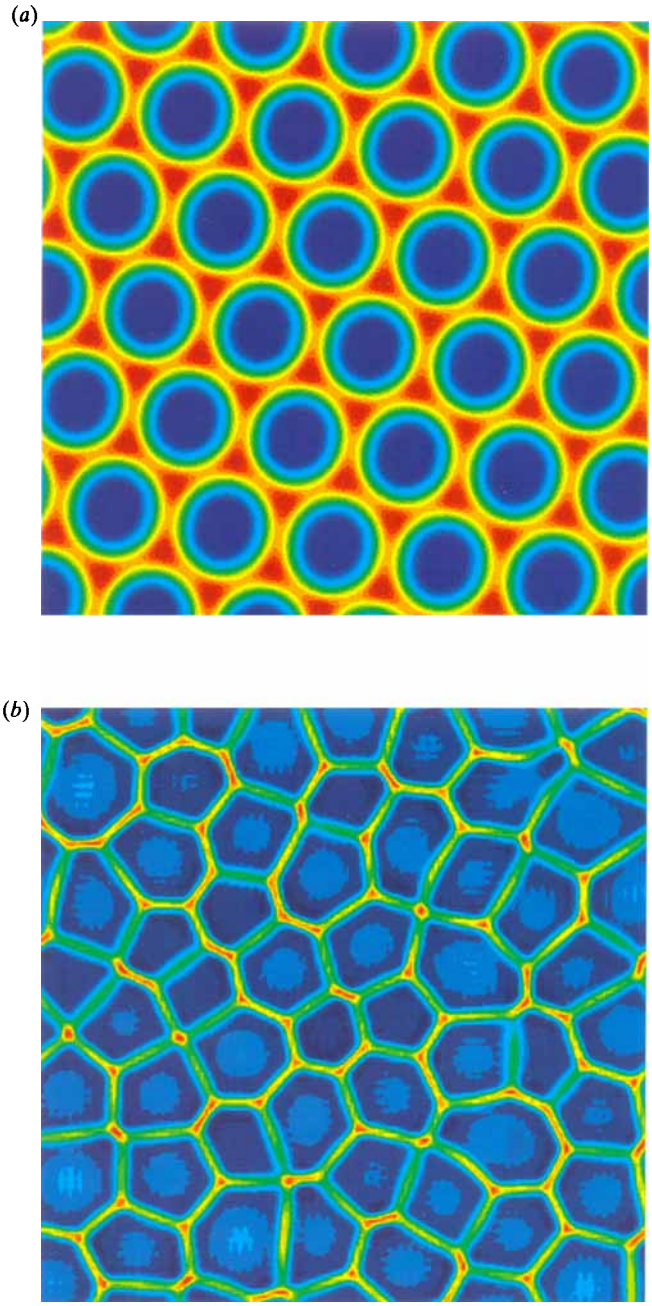

FIGURE 6. Generation of small-scale structures in Bénard–Marangoni convection: plots of $\Delta_2\theta_s(x,y)$ for (*a*)$Ma = 80, t = 1400$; (*b*)$Ma = 150, t = 20$. Aspect ratio is 20, spatial resolution $128^2 \times 32$. Blue [red] corresponds to minimum [maximum] of the field.

Therefore

$$\langle\theta_s(\boldsymbol{r})\,\theta_s(\boldsymbol{r}')\rangle = \frac{N\bar{J}^2}{4\pi^2}\int\frac{e^{ik(r-r')}}{k^4}\,d^2k - \frac{(N\bar{J})^2}{2}\int\frac{\delta(\boldsymbol{k})}{k^4}e^{ik(r-r')}\,d^2k. \tag{50}$$

Comparing this with the definition $\int E(k)\,dk = \langle\theta^2\rangle/2$ leads to the result

$$E(k) = N\bar{J}^2/(2\pi k^3) \tag{51}$$

valid in the 'inertial' range $1/l < \log(k) < 1/\delta$. The proper representation of the detailed structures of the temperature derivatives requires high numerical resolution, and it is not surprising that the limiting spectrum can be reached only approximately. In order to test the assertion about the crucial importance of the plumes, we have made simulations for a different geometry, i.e. a narrow strip $0 < x < 3$, $0 < y < 0.3$. In this geometry a quasi-one-dimensional structure of rolls aligned with the y-axis forms without plumes and produces a spectral exponent $\alpha = 4.25$ which is close to 4 as is to be expected from one-dimensional curvature singularities.

5.3. *On the validity of amplitude equations*

In the past, direct simulation of large-aspect-ratio pattern formation in fluids was beyond the capacity of computers. Nonlinear amplitude equations, derived from the hydrodynamic equations under the simplifying assumptions of weak supercriticality and slow space–time variation, were the only feasible theoretical approach to large-aspect-ratio pattern formation. In many cases they were used beyond their mathematical limit of validity without the possibility to assess their predictive power.

The present numerical simulation permits the testing of the nonlinear model equation

$$\theta_t + \tfrac{1}{15}\theta_{xxxx} + b\theta + \epsilon[\theta_x - \epsilon\tfrac{48}{35}\theta_x^3 + \epsilon\tfrac{13}{10}\theta_x\theta_{xx}]_x = 0 \tag{52}$$

derived by Sivashinsky (1982) for Bénard–Marangoni convection on the basis of a long-wave expansion. The model equation was obtained under the assumption of a purely two-dimensional motion confined to the (x, z)-plane, governed by equations (23)–(31) with the thermal boundary condition $\theta(0) = 0$ replaced by the phenomenological boundary condition

$$\partial_z\theta(0) - b\theta(0) = 0. \tag{53}$$

Here b can be considered as the Biot number of the bottom. Equation (52) was derived under the additional assumptions that $b \ll 1$ and that $\epsilon = (Ma - Ma_0)/Ma_0 \ll 1$ in which case the application of the multiple-scale perturbation technique allows the problem to be reduced to a one-dimensional equation for the temperature

$$T(x, z) = -z + \theta(x) \tag{54}$$

because the wavelength of the unstable mode tends to zero in the limit $b \to 0$. Our governing equations (23)–(31) formally correspond to the case $b \to \infty$. At first glance, it may not seem a good idea to compare a model with $b \ll 1$ to numerical simulations for $b \gg 1$. Therefore we have performed additional direct simulations of the governing equations with the bottom boundary condition (53) for different values of b, including the cases $b \ll 1$. The results of these simulations show that the particular value of b does not have any significant influence on the nonlinear generation of small-scale structures (cf. figure 5). The value of b only influences the large-scale properties of the convection by favouring larger periodicity lengths which is a linear effect.

We have performed a series of numerical simulations of equation (52) with parameter values $\epsilon \gg 1$ deliberately violating the assumption $\epsilon \ll 1$ of the Sivashinsky

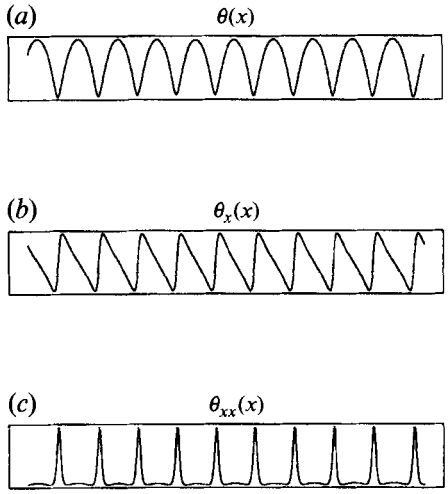

FIGURE 9. (*a*) Stationary solution $\theta(x)$ of the one-dimensional Sivashinsky equation for $\epsilon = 20$, $b = 660$, $N = 2048$, together with the first (*b*) and second (*c*) derivatives.

theory in order to check if the model reproduces the behaviour of the system in the strongly nonlinear regime, at least qualitatively. We use a pseudospectral method with 2048 collocation points in combination with the 'slaved frog' time-stepping scheme (Frisch, She & Thoual, 1986) in order to correctly resolve the dynamics of the small scales, which adiabatically follow the large scales. Random initial conditions are used in all simulations.

Our numerical results, summarized in figure 9, demonstrate that the nonlinear terms of (52) reflect some important aspects of convection. For fixed b, a periodic solution bifurcates supercritically from $\theta = 0$ as soon as $\epsilon > (4b/15)^{1/2}$ with a wavenumber $k = (15b)^{1/4}$. The solution has a sinusoidal shape as long as ϵ exceeds only slightly the critical value. For higher values of ϵ, equation (52) reproduces the formation of discontinuities of the temperature gradient as the essential nonlinear features of the temperature field. The results plotted in figure 9 demonstrate the departure of the temperature from a sinusoidal shape (figure 9*a*), the sawtooth structure of $\partial_x \theta$ (figure 9*b*) and the tendency of the second derivative (figure 9*c*) to develop singularities. We have found that the equation yields the correct one-dimensional spectrum $E \sim k^{-4}$ in the case $\epsilon \gg 1$. Other important features are lost in the course of the derivation. In particular, the Nusselt number, corresponding to the integral over θ, is a conserved quantity and remains zero if it is zero in the initial condition, in contrast to the full problem. The possibility of hydrothermal unstable waves, which are known to exist if the temperature gradient at the free surface become sufficiently high (Smith & Davis 1983), is sacrificed with the simplified ansatz $T = -z + \theta(x)$. It would be interesting to see if higher-order terms in the multiple-scale method used by Sivashinsky can recover this important mechanism for secondary instabilities. Still, the correct reproduction of the one-dimensional temperature spectrum and of the curvature singularities encourages us to recommend the use of the two-dimensional extension of (52), given by Sivashinsky (1982), for the modelling of patterns in Bénard–Marangoni instability, even at high Marangoni numbers. More precisely, the use of the two-dimensional model instead of the three-dimensional equations would allow simulations at much higher lateral resolution thereby giving the possibility to explore the 'inertial range' of the temperature field in more detail.

6. Numerical shadowgraph images – a bridge between theory and experiment

The prediction of a universal spectrum of the surface temperature can be tested in an experiment, albeit not directly. Since the surface temperature itself is not easily accessible to measurements, we shall translate our results into the language of experimental quantities amenable to direct measurements. In previous experimental studies of Bénard–Marangoni convection, shadowgraph methods were used for the flow visualization. Let us briefly recall the basic ideas of this method and derive the relation between the three-dimensional hydrodynamic quantities and the measured two-dimensional distribution of light intensity in the shadowgraph image. Our calculation is a generalization of the work of Jenkins (1988) to the case where the z-dependence of the temperature field is explicitly known.

When a beam of parallel light shines onto an isothermal layer of transparent fluid with a non-deformed surface, the beam is reflected at the bottom $z = 0$ and its image, recorded on a distant screen, has a uniform brightness ρ_0. In the convective state, the inhomogeneous temperature $T(x, y, z)$ and the surface deflection $h(x, y)$ cause the light beams to be deflected. This deflection, yielding a deviation $\delta\rho(x, y)$ from the homogeneous distribution, carries information about the temperature and the surface deformation. The two mechanisms are sketched in figure 10. We shall focus on the temperature field since we consider a non-deformed surface in our model. If the surface is not deformed (figure 10*a*), the trajectory $[x(z), y(z)]$ of a light ray within the non-isothermal fluid is governed by the differential equations

$$\frac{\mathrm{d}^2x}{\mathrm{d}z^2} = -\frac{1}{n_0}\left(\frac{\mathrm{d}n_0}{\mathrm{d}T}\right)\partial_x T(x, y, z), \tag{55a}$$

$$\frac{\mathrm{d}^2y}{\mathrm{d}z^2} = -\frac{1}{n_0}\left(\frac{\mathrm{d}n_0}{\mathrm{d}T}\right)\partial_y T(x, y, z), \tag{55b}$$

where n_0 is the refractive index of the fluid at $T = T_0$ and $\mathrm{d}n_0/\mathrm{d}T$ is the coefficient of temperature dependence of the refractive index, i.e. $n(T) \approx n_0 + (\mathrm{d}n_0/\mathrm{d}T)(T - T_0)$. Equation (55) holds for $(\mathrm{d}n_0/\mathrm{d}T) \ll 1$. For silicone oil $n_0 \approx 1.4$ and

$$dn_0/\mathrm{d}T \approx 10^{-4}\ \mathrm{K}^{-1}.$$

The ray is reflected at the bottom, 2, and leaves the fluid, after having traversed the layer for the second time, at point 3, differing from the entry point 1, by the vector $\boldsymbol{s}_0$ (cf. figure 10*a*). Here $\boldsymbol{n}$ is the direction of the outgoing ray. The image of the ray arrives at the screen, which is supposed to be located at a distance $H \gg d$ from the free surface. The displacement $\boldsymbol{s}_1(x, y)$ completely determines the intensity distribution $\delta\rho(x, y)/\rho_0$ of the shadowgraph pattern. In general, the determination of $\delta\rho/\rho_0$ requires the solution of the system (55) which is nonlinear because T is a function of the space coordinates. Moreover, the relation between $\delta\rho/\rho_0$ and the displacement $\boldsymbol{s}_1$ cannot usually be expressed analytically. Fortunately, an analytical expression for $\delta\rho/\rho_0$ as a function of $T(x, y, z)$ can be given under the simplifying assumption $|\boldsymbol{s}_0| \ll |\boldsymbol{s}_1| \ll 1$ which is satisfied in all experiments. The assumption $|\boldsymbol{s}_1| \ll 1$, which is met due to the smallness of $\mathrm{d}n_0/\mathrm{d}T$, allows us to express the shadowgraph intensity as

$$\delta\rho/\rho_0 = -\partial_x s_{1x} - \partial_y s_{1y}. \tag{56}$$

The assumption $|\boldsymbol{s}_0| \ll |\boldsymbol{s}_1|$, justified by $H \gg d$, allows us to use

$$s_{1x} \approx Hn_x, \quad s_{1y} \approx Hn_y \tag{57}$$

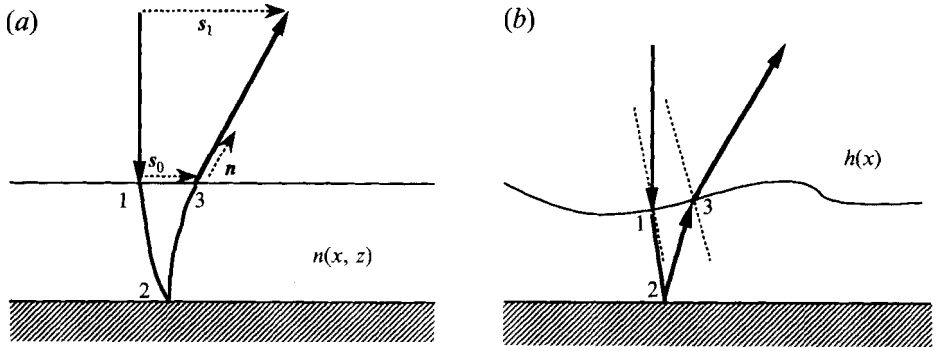

FIGURE 10. Deflection of a beam of light due to (*a*) inhomogeneous temperature distribution, (*b*) surface deflection.

for the determination of s_1 without taking into account the contribution from s_0. Finally, the smallness of $\mathrm{d}n_0/\mathrm{d}T$ permits us to treat $\partial_x T$ and $\partial_y T$ in (55) as functions of z only, evaluated at the entry point (x_0, y_0) of the light ray. Equations (55) can then be solved analytically yielding the trajectory $1 \to 2 \to 3$ in figure 10(*a*) and, taking into account the refraction at the free surface, the components of $\boldsymbol{n}$. With this step done, the shadowgraph field is readily derived as

$$\frac{\delta\rho}{\rho_0} = 2H\left(\frac{\mathrm{d}n_0}{\mathrm{d}T}\right)(\partial_x^2 + \partial_y^2)\int_{z=0}^{z=d} \theta(x, y, z)\,\mathrm{d}z. \tag{58}$$

Here we have used physical variables, and we have replaced T by θ because $\partial_x T = \partial_x \theta$ and $\partial_y T = \partial_y \theta$.

Using elementary rules of geometric optics, the shadowgraph field due to surface deflection $h(x, y)$, sketched in figure 10(*b*), is determined as

$$\delta\rho/\rho_0 = -H(2n_0 - 1)(\partial_x^2 + \partial_y^2)h. \tag{59}$$

In principle, both effects are present in an experiment. We remark parenthetically that the surface deflection can be calculated from the velocity and pressure field at the free surface using the Laplace condition.

Equation (58) reveals that the shadowgraph function is proportional to the two-dimensional Laplacian of the vertically averaged temperature perturbation. Thus, the shadowgraph image has the same spectral properties as the Laplacian of the surface temperature, but is more smooth owing to the averaging in the z-direction. In figure 11 we plot shadowgraph fields obtained from the temperature distributions for $Ma = 80$ and 150 through equation (58). Although the contrast of the small-scale structures is less pronounced than in the plots of $\Delta_2 \theta_s$ (figure 6) the knots between the convective cells are readily seen as intensity maxima. The prediction $E \sim k^{-3}$ for the temperature field implies $E_\rho \sim k$ for the spectrum of the shadowgraph field, which can be tested experimentally.

7. Conclusions and further developments

We have performed direct numerical simulations of Bénard–Marangoni convection. The numerical results demonstrate that the generation of hexagonal convective cells is possible by surface forces alone in agreement with Pearson's (1958) results. The decrease of cell size with increasing Ma for weakly supercritical flows is in qualitative

(*a*)

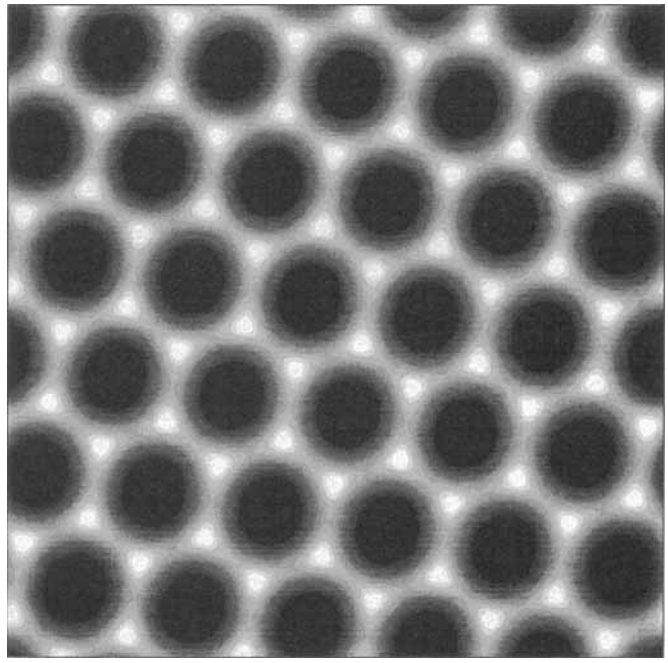

(*b*)

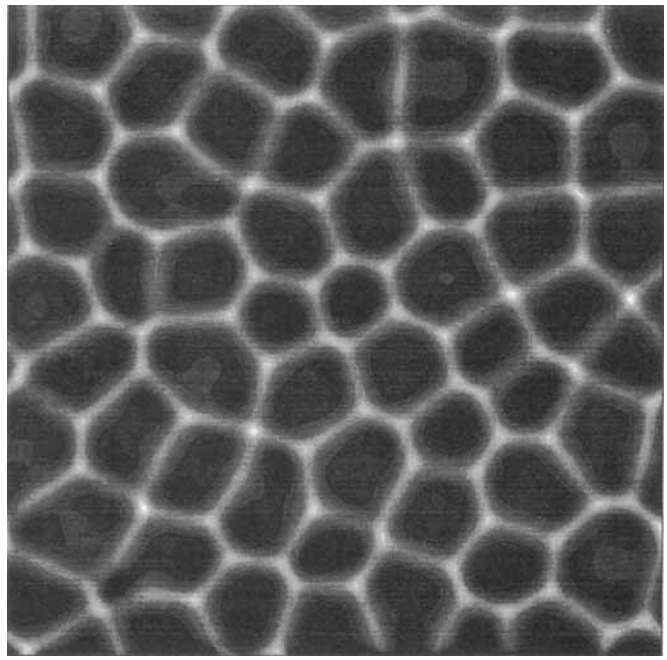

FIGURE 11. Numerically generated shadowgraph images: plots of $\Delta^2 \int_0^1 \theta(x, y, z)\,\mathrm{d}z$ for (*a*) $Ma = 80$, and (*b*) $Ma = 150$. Aspect ratio 20. White [black] corresponds to maximum [minimum] of the field.

agreement with experiments in shallow fluid layers. Our numerical calculations are free of the influence of gravity and constitute therefore a perfect microgravity environment. For some parameter values, they proceed faster than a real-life laboratory experiment. Performed in conjunction with carefully controlled laboratory experiments on Earth, they provide an attractive alternative to expensive microgravity experiments aboard spacecrafts with low availability. The addition of buoyancy forces to our theoretical model, which can be done at slightly increased computational cost, gives the possibility first to test the numerical code by quantitative comparison with experiments and then to use the code to extrapolate the results to the microgravity limit $g \to 0$. Addition of the buoyancy force would also be interesting for a better understanding of the suggestion that gravity is responsible for the fact that the cell size begins to increase when the Marangoni number becomes larger than twice its critical value (Koschmieder & Switzer 1992). We could not find evidence for the existence of flows for subcritical Marangoni numbers as small as reported by Koschmieder & Biggerstaff (1987). The explanation of the latter must be sought in the influence of the surface deformation or buoyancy.

Our numerical simulations permit the study of pattern formation in large-aspect-ratio geometries, thereby giving the opportunity to critically assess the predictive power of nonlinear amplitude equations that have hitherto been considered as the only theoretical tool for the study of pattern formation in fluids. In this paper, we have shown that the Sivashinsky equation (52) is capable of reproducing the generation of the essential nonlinear structures (discontinuities of the temperature gradients) but fails to grasp hydrothermal waves. Since the speed of our numerical computation in comparison with experiments relies on the low Reynolds number of the flow, rather than on particular mathematical features of the theoretical model, our approach can be extended to other pattern-forming convective systems like Rayleigh–Bénard convection, binary convection and thermosolutal convection.

We have demonstrated that for high Marangoni numbers non-trivial small-scale structures are generated in surface-tension-driven Bénard convection which yield a spectrum $E \sim k^{-3}$ of surface temperature. This prediction can be translated into the language of experiments, predicting a spectrum of the shadowgraph pattern proportional to k.

It is important to emphasize that, although the $E \sim k^{-3}$ behaviour holds for a large range of Marangoni numbers, the (mathematical) problem of understanding the asymptotic regime for $Ma \to \infty$ remains unsolved. It is very likely that time-dependent states emerge from the quasi-stationary structures plotted in figure 7 above $Ma \sim 3000$–4000, which is unfortunately beyond our present numerical capabilities. The properties of the $Ma \to \infty$ regime will certainly be different from classical Kolmogorov turbulence, since only the Péclet number tends to infinity whereas the Reynolds number remains small by virtue of the definition of the infinite Prandtl number model. Nevertheless, the following qualitative argument shows that flows with spatio–temporal irregularity are to be expected in this asymptotic regime. If we consider purely two-dimensional solutions to (25), confined to the (x,y)-plane, we can introduce a stream function ψ with $v_x = \partial_z \psi$,, $v_z = -\partial_x \psi$ and rewrite (25) in the form

$$\partial_t \theta - J(\psi, \theta) = -\partial_x \psi + \nabla^2 \theta, \quad \hat{L}_{Ma} \psi = \theta, \tag{60}$$

where $\hat{L}_{Ma}$ is an abbreviation for the Stokes boundary value problem determining the stream function as a function of the temperature perturbation, and $J(f,g)$ is the Jacobian. Equation (60) has a formal analogy to the quasi-geostrophic model

$$\partial_t \omega - J(\psi, \omega) = \beta \partial_x \psi + \nu \Delta \omega, \quad \Delta \psi = -\omega \tag{61}$$

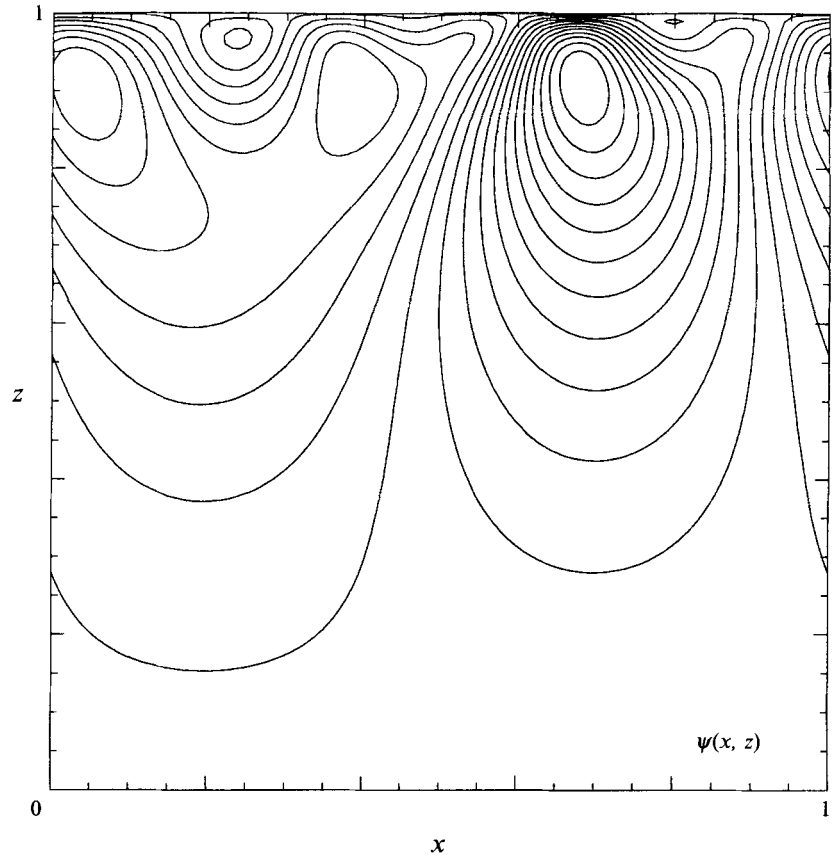

FIGURE 12. Streamlines of a kinematically possible velocity field for random surface temperature.

of two-dimensional atmospheric turbulence. The temperature perturbation formally takes the role of vorticity. While the linear term in (60) is responsible for an instability, the β-term in (61) describes Rossby waves. For $\nu \ll 1$ the solutions to (61) are in general turbulent and similarly 'thermal turbulence' can be expected for sufficiently high Marangoni numbers – for two as well as for three dimensions. Figure 12 shows the streamlines of a velocity field generated by a random surface temperature distribution as solutions of the Stokes problem in Bénard–Marangoni convection. It reveals that the kinematically possible velocity fields can have remarkable complexity, and it is a challenging problem for future studies to understand Bénard–Marangoni convection in the limit $Ma \to \infty$.

It is a pleasure to acknowledge the comments and suggestions of E. L. Koschmieder on a first version of the manuscript. One of us (A.T) is grateful to the Deutsche Forschungsgemeinschaft for financial support under Grant Th 497/2-1. This work was partially supported by the Air Force Office of Scientific Research and the Advanced Research projects Agency under Contracts N00014-92-C-0118 and N00014-93-C-0216. The authors are grateful to V. Borue for providing a part of the numerical code and to K. Nitschke, I. Staroselsky and M. Bestehorn for interesting discussions.

Ma	Bi	λ
70	0	−0.732128060
80	0	0.029661942
90	0	0.780336913
100	0	1.520638207
500	0	26.361959357
1000	0	51.385372968
70	1	−3.168955695
80	1	−2.495744560
90	1	−1.829547320
100	1	−1.170020621
500	1	21.761508688
1000	1	45.525274684

TABLE 2. Growth rates of Bénard–Marangoni instability calculated from linear stability theory for infinite Prandtl number and $k = 2$

Appendix. Growth rates of the primary instability

We wish to compute the growth rate $\lambda(k, Ma, Bi)$ of infinitesimal perturbations of the form

$$v_x = \epsilon \frac{\mathrm{i}}{k} \mathrm{e}^{\lambda t + \mathrm{i}kx} \mathrm{D}W(z), \tag{A 1}$$

$$v_z = \epsilon \mathrm{e}^{\lambda t + \mathrm{i}kx} W(z), \tag{A 2}$$

$$\theta = \epsilon \mathrm{e}^{\lambda t + \mathrm{i}kx} G(z), \tag{A 3}$$

with $\mathrm{D} = \mathrm{d}/\mathrm{d}z$ and $\epsilon \to 0$. This is a generalization of Pearson's (1958) calculation of the neutral curve $Ma(k, Bi)$ from the assumption $\lambda = 0$. The linear stability problem derived from the governing equations (23)–(31) is

$$(\mathrm{D}^2 - k^2)^2 W = 0 \tag{A 4}$$

$$[\lambda - (\mathrm{D}^2 - k^2)] G = W, \tag{A 5}$$

with the boundary conditions

$$W(0) = \mathrm{D}W(0) - W(1) = \mathrm{D}^2 W(1) + Ma\, k^2 G(1) = 0, \tag{A 6}$$

$$G(0) = \mathrm{D}G(1) + BiG(1) = 0. \tag{A 7}$$

In principle, the desired growth rate can be obtained by writing down the general solution of (A 4) and (A 5), enforcing boundary conditions (A 6) and (A 7) to derive a system of six linear equations for the six unknown coefficients, and requiring the determinant of the corresponding matrix to be zero. However, the solution can be accomplished in a slightly more elegant fashion owing to the particular structure of the boundary conditions.

Since the problem is linear, we can freely choose the amplitude of either W and G. The particularly convenient gauge

$$G(1) = 1/(Mak^2) \tag{A 8}$$

allows us to eliminate the temperature perturbation from the equations for W, which can then be solved explicitly as

$$W(z) = w_1 \sinh(kz) + w_2 z \sinh(kz) + w_3 z \cosh(kz) + w_4 \cosh(kz). \tag{A 9}$$

The coefficients are determined by the boundary conditions (A 6) and $w_4 = 0$. Knowing W, we solve (A 5) for G which yields

$$G(z) = \frac{w_1}{\lambda}\sinh(kz) + w_2\left[\frac{z}{\lambda}\sinh(kz) + \frac{2k}{\lambda^2}\cosh(kz)\right] + w_3\left[\frac{z}{\lambda}\cosh(kz) + \frac{2k}{\lambda^2}\sinh(kz)\right] + g_1\sinh[(k^2+\lambda)^{1/2}z] + g_2\cosh(k^2+\lambda)^{1/2}z]. \quad \text{(A 10)}$$

The coefficients g_1 and g_2 of the homogeneous solution are determined by the boundary conditions (A 7). The desired growth rate is obtained by requiring $G(1)$ as calculated from (A 0) to satisfy the assumption (A 8), from which we derive the implicit expression

$$F(\lambda, k, Ma, Bi) \equiv G(1) - \frac{1}{Mak^2} = 0. \quad \text{(A 11)}$$

The expressions for the coefficients w_1, w_2, w_3, g_1, g_2 as functions of λ, k and Bi can be readily derived and shall not be given here. Equation (A 11) is solved numerically by finding zeros of $F(\lambda)$ for given values of k, Ma and Bi. The results are summarized in table 2.

REFERENCES

BÉNARD, H. 1900*a* *Rev. Gén. Sci. Pures Appl.* **11**, 1261–1268.

BÉNARD, H. 1900*b* *J. Phys. Paris* **IX** (3), 513–524.

BENSIMON, D. 1988 *Phys. Rev.* A **37**, 200–206.

BESTEHORN, M. 1993 *Phys. Rev.* E **48**, 3622–3634.

BLOCK, M. J. 1965 *Nature* **178**, 650–651.

BRAGARD, J. & LEBON,G. 1993 *Europhys. Lett.* **21**, 831–836.

CANUTO, C., HUSSAINI, M., QUARTERONI, A. & ZHANG, T. 1987 *Spectral Methods in Fluid Dynamics.* Springer.

CASTAIGN, B., GUNARATNE, G., HESLOT, KADANOFF, L., LIBCHABER, A., THOMAE, S., WU, X.-Z., ZALESKI, S. & ZANETTI, G. 1989 *J. Fluid Mech.* **204**, 1–30.

CERISIER, P., PEREZ-GARCIA, P., JAMOND, C., PANTALONI, J. 1987 *Phys. Rev.* A **35**, 1949–1952.

CERISIER, P., PEREZ-GARCIA, P. & OCCELLI, R. 1993 *Phys. Rev.* E **47**, 3316–3325.

CLOOT, A. & LEBON, G. 1984 *J. Fluid Mech.* **145**, 447–469.

DAVIS, S. H. 1969 *J. Fluid Mech.* **39**, 347–359.

DAVIS, S. H. 1987 *Ann. Rev. Fluid Mech.* **19**, 403–435.

FRISCH, U., SHE, Z. S. & THOUAL, O. 1986 *J. Fluid Mech.* **168**, 221–240.

GOTTLIEB, D. & ORSZAG, S. A. 1978 *Numerical Analysis of Spectral Methods.* CBMS-NSF Regional Conference Series in Applied Mathematics, Philadelphia.

GRODZKA, P. G. & BANNISTER, T. C. 1972 *Science* **176**, 506–508.

GRODZKA, P. G. & BANNISTER, T. C. 1975 *Science* **187**, 165–167.

JENKINS, D. R. 1988 *J. Fluid Mech.* **190**, 451–469.

KOSCHMIEDER, E. L. 1967 *J. Fluid Mech.* **30**, 9–15.

KOSCHMIEDER, E. L. 1991 *Euro. J. Mech.* B (*Fluids*) **10**, 233–237.

KOSCHMIEDER, E. L. 1993 *Bénard Cells and Taylor Vortices.* Cambridge University Press.

KOSCHMIEDER, E. L. & BIGGERSTAFF, M. I. 1986 *J. Fluid Mech.* **167**, 49–64.

KOSCHMIEDER, E. L. & SWITZER, D. W. 1992 *J. Fluid Mech.* **240**, 533–548.

LANDAU, L. D. & LIFSHITZ, E. M. 1987 *Fluid Mechanics.* Course of Theoretical Physics, vol. 6. Pergamon Press.

NEWELL, A. C., PASSOT, T., & LEGA, J. 1993 *Ann. Rev. Fluid Mech.* **25**, 399–453.

NIELD, D. A. 1964 *J. Fluid Mech.* **19**, 341–352.

NORMAND, C., POMEAU, Y. & VERLARDE, M. G. 1977 *Rev. Mod. Phys.* **49**, 591–624.

OCCELLI, R., GUAZZELLI, E. & PANTALONI, J. 1983 *J. Phys. Lett.* **44**, 567–580.

PEARSON, J. R. 1958 *J. Fluid Mech.* **4**, 489–500.

RATH, H. J. (ed.) 1992 *Microgravity Fluid Mechanics*. Springer.

SAFFMAN, P. G. 1971 *Stud. Appl. Maths* **50**, 377–383.

SCANLON, J. W. & SEGEL, L. A. 1967 *J. Fluid Mech.* **30**, 149–162.

SCHUBERT, G. 1992 *Ann. Rev. Fluid Mech.* **24**, 359–394.

SCRIVEN, L. & STERNLING, C. 1964 *J. Fluid Mech.* **21**, 321–340.

SIVASHINSKY, G. I. 1982 *Physica* D **4**, 227–235.

SMITH, M. K. & DAVIS, S. H. 1983 *J. Fluid Mech.* **132**, 119–144.

THESS, A. & ORSZAG, S. A. 1994 *Phys. Rev. Lett.* **73**, 541–544.

TRAVIS, B., OLSON, P. & SCHUBERT, G. 1990 *J. Fluid Mech.* **216**, 71–91.

VERLARDE, M. G. (ed.) 1988 *Physicochemical Hydrodynamics*. NATO ASI Series, vol. 174, Plenum Press.

VERLARDE, M. G. & CASTILLO, J. L. 1981 In *Convection Transport and Instability Phenomena* (ed. J. Zierep). Braun-Verlag.

VINCENT, A. P. & YUEN, D. A. 1988 *Phys. Rev.* A **38**, 328–334.

WHITEHEAD, J. A. & PARSONS, B. 1978 *Geophys. Astrophys. Fluid Dyn.* **9**, 201–217